https://doi.org/10.1038/s44182-025-00028-1

A soft robotic "Add-on" for colonoscopy: increasing safety and comfort through force monitoring

Viola Del Bono[1,6], Max McCandless[1,6], Arincheyan Gerald[1], Emma Capaldi[1], Johann Pang[2], Casper Muter[1], Mark Baldiswieler[1], Hiroyuki Aihara[3] & Sheila Russo[1,4,5] ✉

Colonoscopy is vital for diagnosing colorectal cancer, but limitations in instrument dexterity and sensor feedback can affect safety and patient comfort. We propose a disposable soft robotic "add-on" that attaches to existing endoscopic tools, enhancing safety without requiring custom instruments or workflow changes. The robot features soft optical sensors for 3D shape detection and force monitoring. If excessive force is detected, soft actuators redistribute pressure. A graphical interface provides real-time force data alongside the endoscope camera view. Validation experiments show accurate 3D shape reconstruction (8.51% curvature error, 9.67% orientation error) and force estimation up to 6 N with 3.38% accuracy. In-vitro tests confirm effective force redistribution, while ex-vivo tests on a bovine colon demonstrate smooth integration with minimal impact on the user learning curve. In-vivo swine studies validate safety and feasibility, confirming compatibility with existing tools and minimal disruption to clinical workflows, ensuring an efficient colonoscopy experience.

Colonoscopy is a key diagnostic and therapeutic procedure for gastrointestinal diseases and is essential for detecting colorectal cancer, polyps, and other abnormalities within the colon. In the United States, colorectal cancer (CRC) is the third most commonly diagnosed cancer and third-leading cause of cancer-related deaths in men and women[1]. However, it ranks second in cancer-related deaths overall and is the leading cause of cancer death in men younger than 50 years of age[2]. Similar statistics are reported for the European Union, with CRC being the second cause of death in men and third in women among cancers, in 2022[3]. The incidence and mortality rates of colorectal cancer have shown a decline over the past few decades, largely due to increased screening and improved treatment options[4]. Regular screening is critical in early detection and prevention, significantly reducing the mortality rate associated with this type of cancer[5]. Despite its critical role in gastrointestinal healthcare, colonoscopy is still a challenging procedure. Patients may experience discomfort and anxiety related to the preparation process, which involves bowel cleansing and fasting, and to the procedure itself. In fact, the limited dexterity and lack of sensor feedback in current endoscopes hinders instrument controllability, which can make navigation challenging and painful for the patient[6]. This leads to poor compliance to screening recommendations[7], which results in failure of early cancer detection, and finally in higher rates of colon cancer[8]. Furthermore, the procedure itself carries risks, including perforation, bleeding, and adverse reactions to sedatives[9,10]. The effectiveness of a colonoscopy is also heavily dependent on the quality of bowel preparation and skills of the endoscopist, leading to variability in detection rates[11]. False negatives can occur, particularly for flat or small lesions, potentially delaying critical diagnoses. Additionally, accessibility and cost issues can limit patient adherence to recommended screening schedules[12].

Several research papers explore advancements in colonoscopy robots, aiming to address the limitations of traditional procedures[13,14]. Wireless capsule endoscopes offer a non-invasive alternative for screening[15–19]. These capsules can capture images of the entire digestive tract as they move through it naturally. However, they present limitations, such as potentially incomplete visualization of the colon, limited battery life, lack of capability for therapeutic interventions, no movement or speed control, and high cost[20–22]. Magnetically guided colonoscopy has also been explored with the aim to provide a more precise control and navigation through the colon, potentially reducing discomfort and improving the accuracy of the procedure[23,24]. Recent literature includes autonomous[25,26], and semi-autonomous[27,28] solutions. However, these technologies require bulky and expensive equipment, which is often not supported by many medical infrastructures, especially in low-income countries, limiting access to these

[1]Mechanical Engineering Department, Boston University, Boston, MA, 02215, USA. [2]Biomedical Engineering Department, Boston University, Boston, MA, 02215, USA. [3]Brigham and Women's Hospital, Harvard Medical School, Boston, MA, 02215, USA. [4]Materials Science and Engineering Division, Boston University, Boston, MA, 02215, USA. [5]Center for Information & Systems Engineering, Boston University, Boston, MA, 02215, USA. [6]These authors contributed equally: Viola Del Bono, Max McCandless. ✉e-mail: russos@bu.edu

tools[29]. Soft robots have been proposed as both assistive devices for endoscope insertion[30,31], and alternative colonoscopy platforms such as self-propelling robots[32–34], balloon-based robots[35–37], and over-the-tube soft devices[38–40]. The advantage of soft robotics approaches lies in their inherent safety due to the use of compliant and biocompatible materials, which makes them well-suited for medical applications[41]. However, in some of the devices proposed, their design inhibits the possibility to have instrument insertion[33,35,36]. The majority of the systems proposed are still at early stages, and only a few systems have achieved an advanced development stage to obtain CE or FDA mark[13]: Aer-o-Scope GI-View (2021), Neoguide System (2009), ColonoSight (2008), Invendo Medical GmbH (2017), and Endotics System from Era Endoscopy (2011). Nevertheless, with the exception of the Endotics System that is available in clinical practice, these systems are not yet on the market[42].

Despite all the technological advancements in the field, force sensing is still an unexplored area in colonoscopy. Monitoring contact forces exerted on the colon wall during navigation is crucial for many aspects. First, excessive force during colonoscopy can lead to perforations or tears in the colon, as well as heavy bleeding, being a risk for the patient safety[43]. By providing real-time feedback on the amount of force being applied, force sensors can help minimize trauma, and also increase comfort for the patient. Second, force sensing can provide a real-time feedback to the endoscopist that could potentially dynamically adjust their technique, leading to a more accurate procedure. Such technology could also be used as a training tool for new clinicians, helping them develop a better understanding of the appropriate force levels needed for a successful and painless procedure. For experienced users instead, real-time feedback on force application could serve as a valuable learning tool, helping them refine their techniques and improve their skills. Lastly, a large database with measured forces during navigation could be created, providing a useful platform for researchers in the field, and informative for clinicians. Attempts to sensorize endoscopes have been performed by using external load cells[44] and force-torque sensors[45,46], but these solutions often result in bulky components and loss of accuracy due to the distance from the sensor and the tissue area being pressed. Piezoresistive technologies have been implemented in[47,48], showing promising results, although they are associated with manufacture complexity, medium-high cost, and challenges in durability and reliability over repeated use and sterilization cycles. Tactile sensing has also been explored[39], where a strain-based sensor is incorporated into a soft balloon to improve polyps diagnosis, but does not aid in safer navigation or force monitoring.

In this paper, we aim to tackle the technical challenges previously mentioned by developing a soft robotic platform that can detect in real-time the force exerted on the colon tissue during colonoscopy, as well as automatically deploy soft actuators to minimize the risk of complications. Additionally, a graphic user interface (GUI) displays the force data and the status of the actuators in real-time (Fig. 1A). The robot consists of a fully-soft sleeve that can be mounted on traditional endoscopes, exploiting soft optical sensing to detect its shape, and ultimately, externally applied force. Whenever an excessive force is detected, the soft actuators inflate, with the aim of redistributing the applied force on a larger area of the colon to improve safety. A portable control box containing the optical circuit and actuation unit was developed in order to be easily transported and installed in endoscopy units. Sensing and actuation were first characterized in order to develop an accurate algorithm to estimate the sleeve pose and contact force, and ultimately control the inflation deployment. After validating the accuracy of shape and force reconstruction, we performed in-vitro tests to assess the actuators performance. To evaluate the robot's operation and functionality in real tissue, we conducted ex-vivo tests with a total of seven users, both novice and experienced. These tests demonstrated the seamless integration of the robot with the clinical workflow, and provided a valuable user feedback on learning curve assessment, as well as mental and physical workload associated with the presence of the robot in the procedure. Lastly, to further demonstrate the safety and effectiveness of our platform in clinically relevant scenarios, two experienced endoscopists successfully performed in-vivo tests on two swines.

Results

Soft robotic sleeve design

The design and working principle of our robot are inspired by our previous proof-of-concept work[49], where we demonstrated the potential of soft optical sensing for force monitoring, focusing on the design, characterization, and bench-top testing of a preliminary device. An overview of the soft robotic sleeve and its cross-section are shown in Fig. 1B, and Supplementary Video 1. The device embeds five soft optical waveguides (WGs) and three pneumatic actuator lines symmetrically spaced 120° apart in order to evenly distribute pressure on the tissue, when inflated. The robot has an outer diameter (OD) of 23 mm and an inner diameter of 12.5 mm, designed to fit on a standard, commercially available endoscope of 12 mm OD (EC-760R-V/L, Fujifilm Medical Systems). Therefore, the resulting system (endoscope + sleeve) results in a diametfer increase of 11 mm with respect to the endoscope alone, with 5.5 mm corresponding to the sleeve added thickness. Despite the increase of size, the total system OD of 23 mm is in line with similar devices proposed in the literature, such as a 20 mm magnetic flexible endoscope, smoothly tested up to in-vivo[25], 26 mm soft add-on devices[30,38,39], and self-propelling colonoscopes of 17.5 mm[32], 22 mm[33], and 26 mm[31]. Furthermore, among the FDA-approved robotic systems mentioned in **Introduction**, the Neoguide colonoscope has a proximal shaft diameter of 20 mm, the Endotics System features a diameter of 17 mm, and the Aeroscope measures 19 mm[24]. Based on the guidance provided by our clinical collaborator, the soft sleeve is strategically positioned directly behind the steerable tip of the endoscope (see Fig. 1B), as this section is where significant

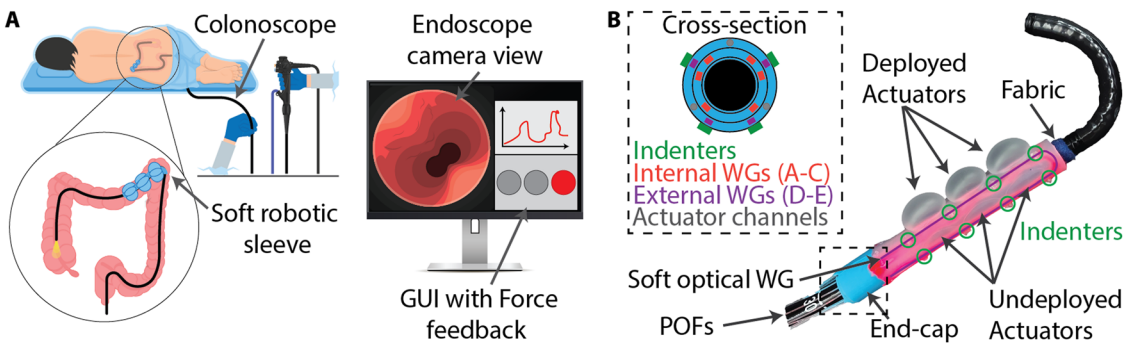

Fig. 1 | Enhanced colonoscopy with the soft robotic sleeve. A The robot, mounted on a commercial endoscope, inflates when a high contact force is detected, reducing patient discomfort and risk of tissue perforation. The force feedback is displayed on a GUI in real time. **B** Soft robotic sleeve overview showing both inflated and deflated actuator lines. An external U-shaped optical waveguide is highlighted in purple along with its set of indenters, circled in green. The stiffer end-cap encapsulates the connection between the soft waveguides and the plastic optical fibers (POFs). The internal fabric layer ensures a low friction when inserted onto the endoscope. The cross-sectional view depicts the layout of the five waveguides (three internal and two external), indenters, and actuation channels.

contact forces are most likely to occur, posing a potential risk of tissue damage and pain[47,50].

The five WGs are separated into two stacked layers: an internal one, which contains three sensors (bending layer, represented by the red WGs (A–C) in the cross-section of Fig. 1B), and an external one, which contains two WGs (contact layer, represented by the purple WGs (D-E) in the cross-section of Fig. 1B). The two top WGs incorporate a set of eight indenters each (circled in green in Fig. 1B), with the aim to amplify the distributed load sensed from the robot, and thus increasing its sensitivity to contact forces. The indenters are secured in place by a thin layer of silicone adhesive (see **Fabrication**), that also acts as a protective soft interface with the tissue, adding a local thickness of only 2 mm to the system. The contact force amplifying indenters are a crucial design aspect, since they exploit the multimodal nature of the waveguides, where a single signal can be used both to detect bending and force, by selectively amplifying different loss modes of the sensors depending on the desired configuration. The robot body is fabricated primarily of Ecoflex™ 00-30. The WGs are surrounded by a layer of DragonSkin™ 30 (anti-buckling layer described in **Fabrication**). These two materials act as optical cladding for the five WGs, while the cores are fabricated from Norland Optical Adhesive 65 (NOA 65), which is a liquid photo-polymer that cures under UV exposure. Thanks to a large difference between the refractive indexes of the cladding and the core material, the resulting critical angle for total internal reflection is $\theta_c = 64.7°$ (Supplementary Equation 1), leading to a high light transmittance. The optical sensing physics is further discussed in Supplementary Text and Supplementary Fig. 1. Dragon Skin™ 30 was utilized as an end-cap material at the base of the sleeve, visible in cyan in Fig. 1B, to stably incorporate the connection between the soft optical waveguides and the rigid plastic optical fibers (POFs) connected to them, that carry the sensor signal to the optical circuit. It also has the function to avoid cross talk between the WGs, as the cyan dye absorbs red light (used as input light source) from exhibiting cross talk. An internal layer of flexible fabric, which reduces friction, allows the system to be easily slid onto a commercial colonoscope. The optical circuit is contained in an external box (30.5 cm × 30.5 cm × 20 cm), along with the actuation unit to inflate the actuators when needed. The control box layout is described in Supplementary Fig. 2. The overall robotic platform, consisting of the soft sleeve and the control box, is designed to be compact and easily transportable into clinical settings. The POFs extending from the robot can be smoothly plugged in and out of the optical circuit, in order to enable an effortless and time-effective setup preparation in the endoscopy unit.

Sensor decoupling algorithm and actuation strategy

Commercial endoscopes are manually guided by the endoscopist, who feeds the tool into the colon and controls the two bending degrees of freedom (DOFs) of the steerable tip. This causes the endoscope to bend in the 3D space, and also to contact the colon lumen. Given their nature, soft optical WGs are sensitive to different types of deformation (i.e., bending, stretching, pressing). For our goal of ultimately measuring contact forces, it is essential to discriminate between optical losses due to bending in the 3D space and optical losses due to contact force (Supplementary Fig. 1), since they happen simultaneously during navigation.

A logic algorithm, that ultimately controls the state of the actuators, was developed in order to decouple the sensor responses of the five optical WGs to estimate the curvature (κ) and orientation (ϕ) of the robotic sleeve as well as the contact force (F) exhibited on the system by its environment. Curvature and orientation combined together give information on the shape of the system in the 3D space. Optical power loss (P) is the attenuation or change in the intensity of the light (I) from its baseline or undeformed value (Io) through a WG and is defined as:

$$P = 10 \cdot \log_{10}(I_o/I) \tag{1}$$

The sensor logic developed is shown in the gray section of the block diagram of Supplementary Fig. 3, and it is based on comparing the live sensor loss of different combinations of WGs to their loss profiles acquired during the calibration processes, both for bending and contact force (see **Curvature and orientation calibration** and **Contact force calibration**). That is, the five WGs (labeled A-E) are used to determine the three coupled DOFs of the system by generating polynomial functions to fit the calibration data:

$$[\kappa, \phi, F] = f[P_A, P_B, P_C, P_D, P_E] \tag{2}$$

where WG A-C are the inner bending layer and D-E are the outer contact layer WGs (see Fig.1B and Supplementary Fig. 4). In order to determine contact force, we must first differentiate the loss of the system due to curvature at different orientations. We recorded the robot's response to bending at curvatures up to 15 m^{-1} (≈ 140°) in 12 different orientations (30° increments, see **Curvature and orientation calibration** and Supplementary Fig. 5) to understand how each WG responds in those bending planes. As discussed in Materials and Methods (**Curvature and orientation calibration**), given the pattern in the loss responses due to the partially symmetrical layout of our design, four main orientations, that we named functional directions (FDs), were chosen among the twelve tested, and force calibration was performed on them (Contact force calibration and Supplementary Fig. 6). From this test, we determined that for each orientation angle there are at least two WGs that exhibit negligible losses due to the distributed load. Thus, these WGs (the combination of which varies depending on the orientation) can be used to estimate κ and ϕ independently from contact force. For example, the curvature and orientation estimation for each FD can be expressed as functions of specific WGs as follows:

$$\begin{aligned} [\kappa, \phi]_{FD_1} &= g_1[P_C, P_E] \\ [\kappa, \phi]_{FD_2} &= g_2[P_C, P_E] \\ [\kappa, \phi]_{FD_3} &= g_3[P_A, P_D] \\ [\kappa, \phi]_{FD_4} &= g_4[P_A, P_D]. \end{aligned} \tag{3}$$

For each loop, the decoupling algorithm estimates the state of the system in either of the four FDs based on the most recent sensor readings (P_{live}) of the chosen sensors in Eq. (3) and determines which estimation yields the minimum error. That is, for each FD, both WGs of each function (g_1−g_4) estimates each other's loss values (P_{pred}) by assuming that the sleeve is truly bent in its FD (e.g, $P_{pred,C} = h[P_{live,E}]$) and then the error ($E$), i.e., the difference between the sum of the estimated and live loss values, is determined as:

$$\begin{aligned} E_1 &= |[P_{pred,C}(P_{live,E}) + P_{pred,E}(P_{live,C})] - (P_{live,C} + P_{live,E})| \\ E_2 &= |[P_{pred,C}(P_{live,E}) + P_{pred,E}(P_{live,C})] - (P_{live,C} + P_{live,E})| \\ E_3 &= |[P_{pred,A}(P_{live,D}) + P_{pred,D}(P_{live,A})] - (P_{live,A} + P_{live,D})| \\ E_4 &= |[P_{pred,A}(P_{live,D}) + P_{pred,D}(P_{live,A})] - (P_{live,A} + P_{live,D})|. \end{aligned} \tag{4}$$

The minimum error is chosen as the correct FD from the error matrix rows 1-4 corresponding to FD_1-FD_4, or written as:

$$FD \Rightarrow \begin{cases} FD_1 & \text{if } E_1 = \min(E_1, E_2, E_3, E_4) \\ FD_2 & \text{if } E_2 = \min(E_1, E_2, E_3, E_4) \\ FD_3 & \text{if } E_3 = \min(E_1, E_2, E_3, E_4) \\ FD_4 & \text{if } E_4 = \min(E_1, E_2, E_3, E_4) \end{cases} \tag{5}$$

such that, for example if E_1 was the minimum error, orientation and curvature can be reconstructed by using the two WGs as in Eq. (3) for FD_1, with the correct function (g_1 in this example) now known. With κ and ϕ determined, we are able to accurately estimate the sensor readings of the other three sensors not utilized in each FD's g function at the orientation

determined, using FD_1 as an example, that is:

$$\begin{aligned} P_{pred,A} &= j_1[\kappa, \phi] \\ P_{pred,B} &= j_2[\kappa, \phi] \\ P_{pred,D} &= j_3[\kappa, \phi]. \end{aligned} \quad (6)$$

However, due to external contact force interactions, these estimations may differ from the actual sensor readings. This discrepancy between estimated and actual sensor readings determines the contact force estimation:

$$F = k[(P_{live,A} + P_{live,B} + P_{live,D}) - (P_{pred,A} + P_{pred,B} + P_{pred,D})]. \quad (7)$$

Ultimately, this logic provides a consistently accurate solution for reconstructing the 3 coupled DOFs and is repeated for each algorithm loop in real-time.

Once the three DOFs (κ,ϕ, F) of the sleeve are established, a strategy was developed and implemented as a MATLAB application in order to trigger the actuation when needed. There are three possible scenarios, as shown in the blue portion of Supplementary Fig. 3: if the force sensed is low (F < 3N), the GUI displays a green indicator; if the force detected is medium-high (3N ≤ F < 5N) the indicator turns yellow to alert the user that they reached a warning zone. Lastly, if excessive force is reached (F ≥ 5N), the actuators are triggered, and the user is alerted by the indicator turning red and by the inflation button turning green. Forces range can vary in colonoscopy procedures[51–53] and can reach up to 40 N[50]. We chose to target a threshold of 5 N for the actuators inflation. This target can be tuned by the endoscopist, depending on their preference and patients' condition. This allows us to prevent excessive forces that could cause severe damage, and also mitigate the pain for the patient. Moreover, a few studies show that the colon can be severely damaged and perforated even at low forces[50], especially when diseased[54]. Given that the actuators reach full inflation in 5 s, we set the inflation time to a total 8 s, to enable the user to navigate with the sleeve fully inflated for an additional 3 s. The determined settling time of 3 s (see **Actuators characterization**) is utilized to return back to baseline sensor signals after inflation, and the system returns to monitoring for excess forces. The layout of the application GUI is reported in Supplementary Fig. 7 and described in Supplementary Material. During the 8 s of inflation time, the sleeve is insensitive to additional contact forces, and data collection is paused. The duration of this time was determined experimentally, based on the average navigation time observed in our experiments. However, it can be adjusted to suit specific procedural requirements. Although this causes the sleeve to not provide continuous feedback during inflation time, measuring additional contact forces during this period is unnecessary, as the inflated chambers create a soft, cushioning effect that acts as a protective barrier and evenly distributes pressure, preventing the risk of additional critical force being applied.

As described in **Soft Robotic Sleeve Design** and visible in Fig. 1, the actuation mechanism is composed by three actuation lines, each of them consisting of a set of three chambers connected to each other. Each line is connected to the actuation unit through a flexible tube, extending from the sleeve and running through the colonoscope together with the POFs. The actuation unit elements are schematized in the orange box of Supplementary Fig. 3. Specifically, The air is supplied by a compressed air source and can be adjusted by a manual pressure regulator. A digital pressure sensor provides input pressure information, and a filter is used to remove any potential dust particle or impurity from the air. A controllable pressure regulator is also used as a safety feature to avoid excessive pressure and to control the actuation status. The inflation mechanism follows a binary control state: if contact force is less than the critical value (5 N), the actuators are kept deflated, whereas if the force reaches or exceeds the critical threshold, air is supplied to the actuators that start to inflate. Please refer to **Actuators characterization** for the actuators characterization. When the chambers are inflated, they create a soft, compliant interface between the endoscope and the colon wall with the aim to redistribute the critical force applied by the endoscope over a larger surface area, thereby reducing localized pressure points. By minimizing concentrated forces, this mechanism helps mitigate the risk of tissue damage, such as perforation or trauma. In this study, we focused on simultaneous chamber inflation to evaluate the effects of full inflation on the procedure and force redistribution. However, the system is versatile, allowing the endoscopist to manually adjust inflation levels and trigger specific chambers as needed. This independent control can enhance safety in clinical scenarios requiring selective inflation on one side of the colon. While such situations did not arise during our ex-vivo and in-vivo tests, this flexibility ensures adaptability to various conditions.

Shape reconstruction validation

A validation experiment was conducted to evaluate the accuracy of the algorithm developed in calculating the shape of the robot in 3D. The latter can be reconstructed by combining the information of the soft optical sensors with a constant curvature modeling approach[55]. As described in **Curvature and orientation calibration**, the sleeve curvature response was calibrated in four functional directions representing sections of the Cartesian plane. Each direction corresponds to the orientation ϕ parameter in the constant curvature model, that is the rotation of the robot around the z-axis. The estimated curvature k_p can be described as:

$$k_p = 1/r_p \quad (8)$$

where r_p is the estimated radius of curvature. These two parameters (κ and ϕ) allow a shape reconstruction of the sleeve as an arc with constant curvature, and they are represented in Fig. 2A. To validate the shape reconstruction, the robot was mounted on the colonoscope and manually moved in the 3D space while recording the sensor signals and its tip position. For the latter, an electromagnetic (EM) tracker (Aurora, Northern Digital Inc.) was used, with a small EM probe fixed at the tip of the soft robot (Fig. 2B). The tip coordinates (x, y, z) recorded by the probe were converted into the actual constant curvature arc parameters (k_a, ϕ_a) by the following trigonometric functions:

$$k_a = \theta/l \quad (9)$$

$$\phi_a = \tan^{-1}(y/x) \quad (10)$$

where $\theta = f(x, y, z)$ is the bending angle (defined by trigonometric rules), and $l = 150\ mm$ is the length of the robot and it is constant. The estimated and actual shape of the robot were compared in terms of κ and ϕ. The results are visible in Fig. 2C, D. The sleeve was sequentially bent up to $\approx 6\ m^{-1}$ towards the four functional directions, corresponding to ϕ= 60°, 120°, 240°, and 300°. The soft robotic sleeve is able to track its own shape in all the workspace (see Supplementary Video 2). In particular, the κ estimation has a mean relative error of 8.51%, while the ϕ estimation has a has a mean relative error of 9.67%, validating the proposed approach. The jitter effect visible in the real-time shape estimation of Supplementary Video 2 is mainly due to the sensor's limited resolution, particularly at low curvatures, where the differences in losses between the 5 WGs are minimal, making it difficult for the algorithm to accurately distinguish between them. In addition, the discretization of the 3D space into four functional directions (described in **Curvature and orientation calibration**) causes the estimated orientation to transition less smoothly, as the algorithm selects among four discrete values, while the manual movement of the sleeve is continuous. These aspects do not prevent accurate force estimation and are further discussed in **Discussion**.

Force estimation validation

The ultimate goal of our robot is to accurately detect contact forces between the endoscope and the colon tissue during colonoscopy navigation. Therefore, we conducted a validation test to evaluate the accuracy of the force estimated by the soft robotic sleeve algorithm. The testing setup is

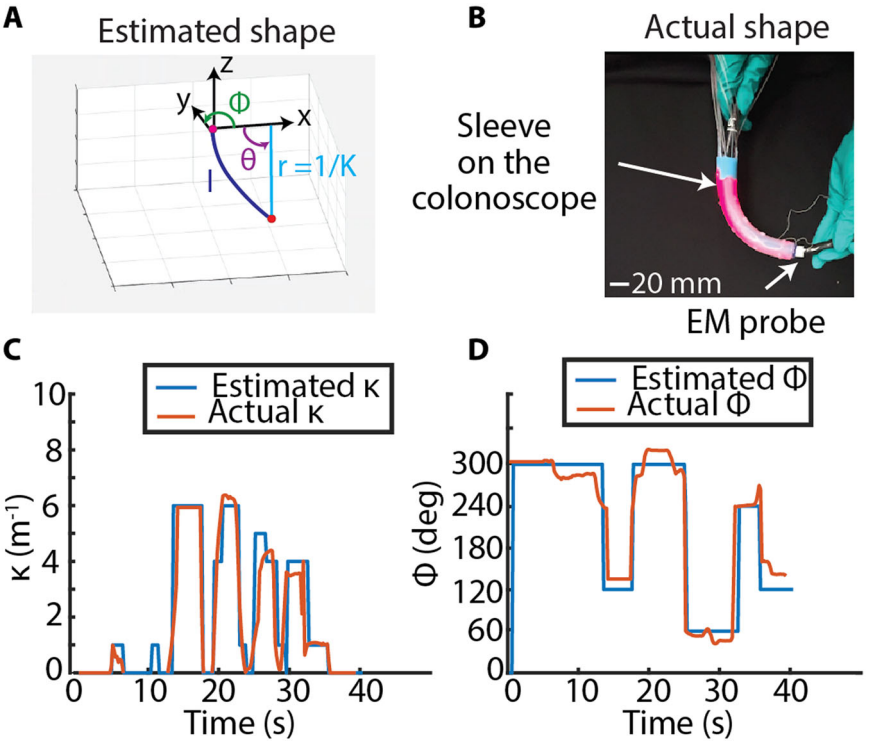

Fig. 2 | 3D shape validation. A Reconstructed shape by using constant curvature modeling. **B** The sleeve tip position is recorded with an EM tracker and subsequently transformed into model parameters k and ϕ. **C**, **D** Comparison between actual and estimated curvature and orientation over time, showing an accurate shape reconstruction throughout the workspace.

presented in Fig. 3A. It includes a robotic manipulator (UR-5, Universal Robots) with a force/torque (F/T) sensor attached to its end-effector (ATI Nano-17, Industrial Automation). Additionally, a curved fixture is mounted on the force sensor to gently push on the robot, simulating a distributed contact, similar to the force calibration process (see **Contact force calibration**). The soft sleeve is mounted on the endoscope and placed on the calibration platform in a straight configuration. From the initial position, the robot is bent up to a 10 m^{-1} curvature. The robot arm is programmed to gently push on the robot, recording the sensor force estimation, and the true force registered by the F/T sensor. This test is repeated by orienting the sleeve in all four functional directions (FDs) in order to capture the estimation in all the 3D spaces.

The results are shown in Fig. 3B (see also Supplementary Video 3). In all the cases, the soft robot is able to accurately estimate the true force applied, with a mean absolute error less than or equal to 0.25 N. Specifically, the calculated estimation errors for each case are reported in Table 1, in terms of mean absolute error and mean relative error. The latter is expressed as sensor accuracy, with a sensing range from 0 N to 6 N. On average, the maximum estimation error found is on FD 2, being 0.25 N, corresponding to a relative percentage error of 4.13%. The minimum error found is on FD 3, corresponding to an absolute error of 0.14 N and a relative percentage error of 2.33%. It is worth mentioning that these small differences in accuracy are due to the manufacturing process, which involves manual placement of the contact amplifying indenters (see **Fabrication**). Overall, the mean absolute error across all the 4 FDs is 0.20 N, while the mean relative error is 3.38%. Nevertheless, the overall force estimation proves to be highly accurate for our purpose, also demonstrating the efficacy of our control algorithm. This is an essential aspect for our robotic platform, since the soft sleeve needs to be able to correctly estimate contact force and subsequently deploy the actuators, if the force reaches the set safety threshold.

Shape validation under external forces

In order to ensure that the shape reconstruction is not affected by the presence of external contact forces, an additional validation has been performed to evaluate the accuracy of curvature and orientation estimations, when an external contact force is applied to the robot. In this experiment, the same setup of **Force estimation** was utilized, including the sleeve mounted on the colonoscope and placed on the calibration board, a robotic manipulator with a F/T sensor attached, and 3D printed curved fixtures to press on the robot (see Fig. 3A). The test consisted of first bending the sleeve up to a certain curvature (5, 7, or 10 m^{-1}), then programming the manipulator to gently press on it, recording both curvature and orientation throughout the whole test, as well as the force applied by the F/T sensor. Finally, external force is removed and the robot is moved back to a straight configuration. This procedure was repeated in all of the four functional directions and the sleeve estimated parameters were compared with the targets. The results are visible in Fig. 4, along with pictures of the sleeve orientation and curvature for each FD tested. In all the cases, the sleeve is able to estimate accurately curvature and orientation even during the application of external contact. The curvature estimation starts from zero with the sleeve straight, gradually reaches the target value, and remains constant during contact until the sleeve is moved back to its (straight) resting position, where the curvature goes back to zero. For the estimated orientation, it is worth noticing that at the beginning and at the end of each test, when the sleeve is straight, all the WG losses are zero because the sleeve is in its baseline configuration, thus any orientation is allowed. Once the sleeve is bent and starts reaching the selected curvature, the orientation adjusts to its target value and remains stable under external contact. The estimation errors for each FDs are calculated for the central section of the test where the sleeve reached its target configuration, and are reported in Table 2. The mean relative errors in predicting the curvature are in line with the previous shape validation (see **Shape reconstruction validation**), and the orientation estimation is highly accurate. These results ultimately prove that the ability of the sleeve to estimate its own shape is not influenced by the presence of external contact, validating the robustness of our algorithm.

In-vitro tests

In-vitro tests were performed on a phantom colon in order to simulate a standard colonoscopy procedure, validating the actuators performance, and the force redistribution on the colon wall during the inflation (see Supplementary Video 4). The phantom colon consists of a 50 mm diameter cylindrical film of thermoplastic elastomer (TPE) (Stretchlon 200,

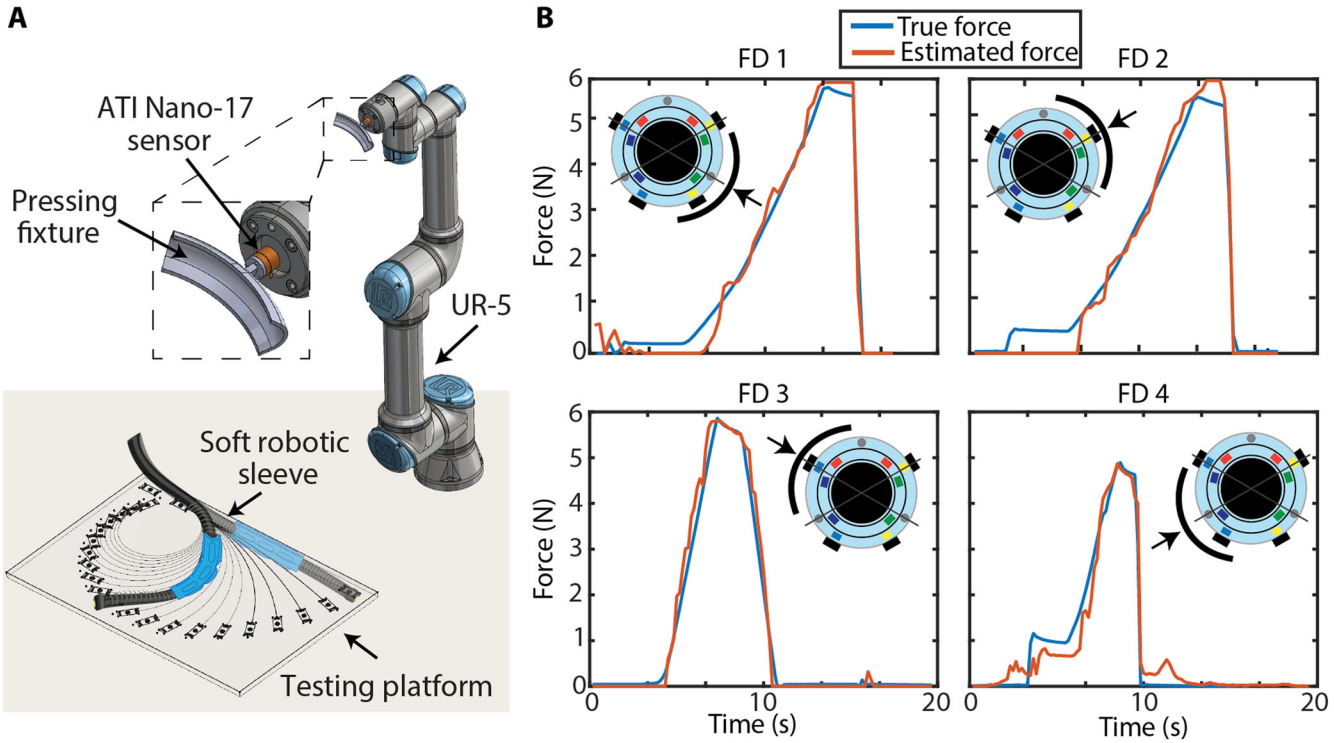

Fig. 3 | Force estimation validation. A Test setup. The soft robot is placed on the curvature testing platform. An ATI-nano 17 force sensor is mounted on the end-effector of a UR-5 robot arm, along with a 3D printed pressing fixture. For each of the calibrated functional directions (FDs), the sleeve is bent up to 10 m^{-1} curvature, and the robot arm gently presses on the soft robot. **B** Estimated versus actual force applied to the soft sleeve in the four FDs. In all cases, the error between the true and estimated force is less than 1 N.

Table 1 | Estimation errors for force validation test

Estimation error	Mean absolute error (*N*)	Mean relative error
FD 1 (60°)	0.23	3.80%
FD 2 (120°)	0.25	4.13%
FD 3 (240°)	0.14	2.33%
FD 4 (300°)	0.19	3.26%
Avg across all FDs	0.20	3.38%

For each functional direction (FD), the mean absolute error and the corresponding mean percentage error are reported. In all cases, the estimation is highly accurate, with an error less than or equal to 0.25 N. The last line represents the average errors across all four FDs.

FibreGlast, USA) inserted into a Kyoto Kagaku Colonoscope Training Model (Kyoto Kagaku Co. Ltd, Kyoto, Japan), as shown in Fig. 5A. TPE film was chosen for its stretchability and transparency. A first set of tests was performed by navigating in the phantom, monitoring the force estimated by the soft robotic sleeve, as well as the actuator status. The navigation was repeated six times, and before starting each test, the sleeve initial position was rotated along the endoscope, in order to make sure that bending will occur in different orientations scenarios (See Supplementary Fig. 8). The user starts navigating with the robot continuously sensing contact forces. In Fig. 5B–D, the three scenarios described in **Soft Robotic Sleeve Design** are reported, corresponding to low, excessive, and medium-high force, respectively. A medical lubricant was used to reduce friction during navigation, as a common practice in colonoscopy. This test ensured the overall functioning of the device, and the ease of navigation with the actuators inflated.

To quantitatively measure the force redistribution due to the actuators inflation, a second experiment was performed. A single 30 cm section of phantom colon was built, and its extremities were secured to two rigid pedestals to avoid possible motion. Three Force Sensing Resistors (FSR-03, Ohmite) were radially attached to the internal lumen and connected to an Arduino (see Fig. 5E). FSRs are particularly suited for this application as they are thin, flexible, and easily attachable to the TPE, without obstructing the simulated colon lumen. The sensors were custom-calibrated up to 10 N, as shown in Supplementary Fig. 9 and Supplementary Text, and their bandwidth was selected from 0 N to 4 N, as the signal saturated after this value. Therefore, the critical pressure for this test was set to 4 N, in order to be in the most sensitive region within the bandwidth of the FSRs. Both the force estimated by the sleeve and the true force measured by the three sensors were recorded throughout the experiment. At the beginning of the test, the endoscope, with the sleeve mounted on it, is inserted into the simulated colon section and held still at its extremities. The user starts pressing on FSR 1, thus increasing its detected force up to the critical threshold, and the actuators are deployed. As visible in Fig. 5F, during this time, the estimated force is following the true force recorded by that sensor, with a mean absolute error of 0.56 N and an average relative error of 9.4%. This error value differs from the accuracy reported in **Force estimation**, due to the manual test conditions and FSRs lower accuracy with respect to the ATI Nano-17. Around 21 seconds, an excessive pressure is reached and the actuators are triggered. The estimated force subsequently goes to zero as the sleeve is pausing data collection during inflation. As the actuators begin to inflate, the set of chambers located between FSR 1 and the colon wall start to push back the endoscope, that straightens (see Supplementary Video 4). This action causes the other actuators to come into contact with FSR 2 and FSR 3. In fact, during this time (between 24 s and 32 s), the force on FSR 1 starts decreasing to an average value of 0.72 N, redistributing to the other sensors, which increase to an average value of 0.73 N and 1.33 N for FSR 2 and FSR 3, respectively. Given that during the test, the colonoscope was held stationary at its ends without active movement, we attribute this effect to the inflation-induced load balancing. These results ultimately prove the hypothesis of force redistribution along the colon phantom circumference.

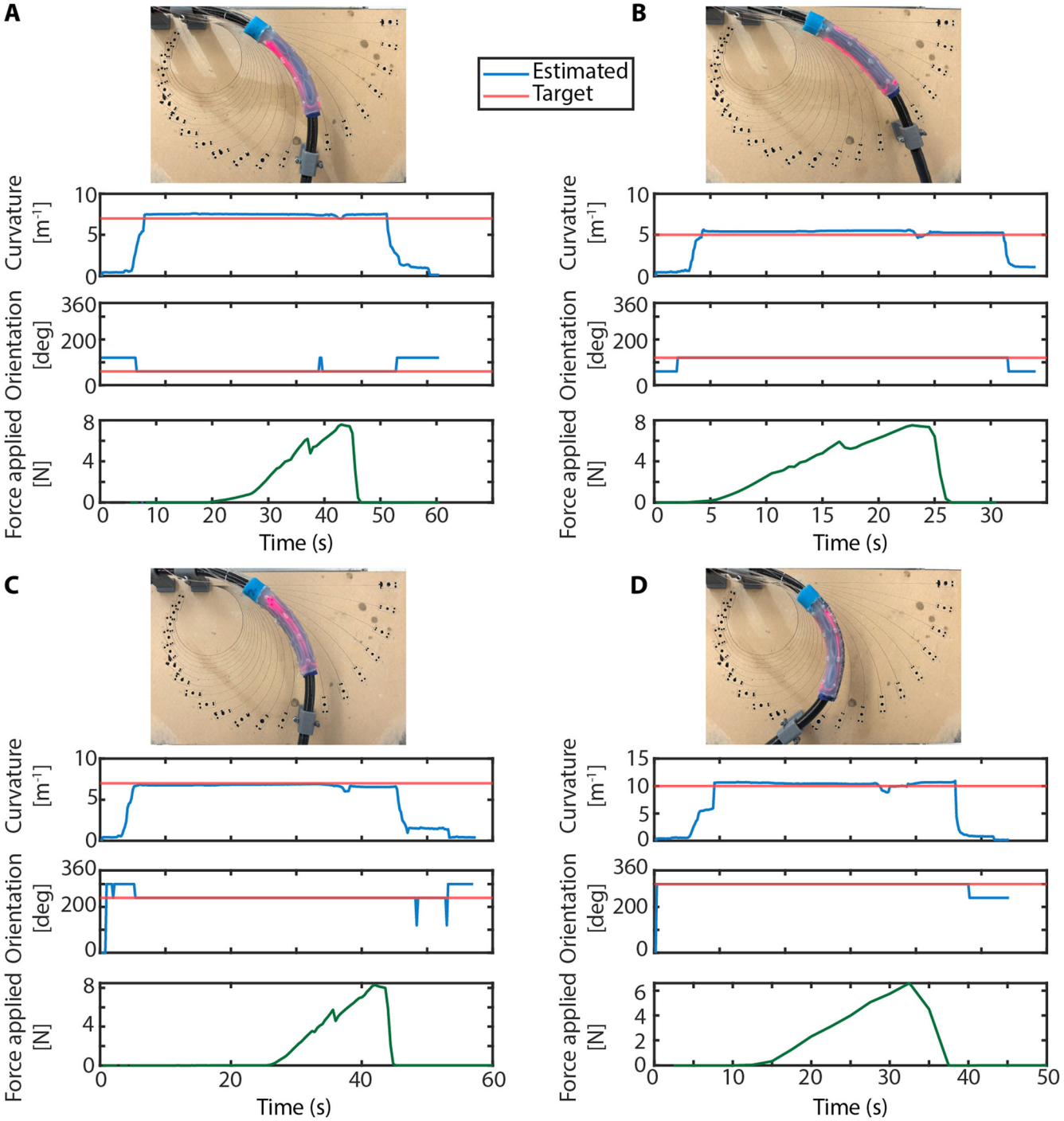

Fig. 4 | Shape estimation under external forces. A Sleeve bent at 7 m^{-1} and oriented at 60° (FD 1). **B** Sleeve bent at 5 m^{-1} and oriented at 120° (FD 2). **C** Sleeve bent at 7 m^{-1} and oriented at 240° (FD 3). **D** Sleeve bent at 10 m^{-1} and oriented at 300° (FD 4).

Ex-vivo tests

Although informative, in-vitro tests are not fully able to replicate clinical conditions, such as tissue elasticity, stiffness, and natural lubrication. Moreover, in order to integrate the robot into an existing procedural workflow, it is essential to assess its ease of use and potential impact on navigation time and the learning curve of endoscopists. In order to evaluate how the integration of the soft robot would be beneficial for colonoscopy navigation, a user study with subjects with different experience in colonoscopy can provide valuable feedback on device acceptance, ease of use, and also a range of data on forces exerted during the navigation.

We conducted an ex-vivo study including a total of seven users, consisting of four novice and three experts (see Supplementary Video 5). The test consisted of a simulated colonoscopy in an explanted bovine colon. The tissue specimen was placed into a ColoEASIE-2 Simulator (Endosim LLC) to mimic the anatomical regions of the human colon (Fig. 6A). The length of the specimen was approximately 60 cm. An external camera was placed above the setup to video-record each test. Each user performed five trials without and with the soft robotic sleeve attached on the colonoscope (n = 35 total trials for each scenario). The time taken for completing each navigation was recorded. When navigating without the soft robotic sleeve, the user has only the visual feedback provided by the endoscope camera, displayed on a

Table 2 | Estimation errors for shape validation under external force

Estimation error	Curvature mean relative error	Orientation accuracy
FD 1 (60°)	6.91%	98.92%
FD 2 (120°)	7.84%	100%
FD 3 (240°)	3.68%	99.55%
FD 4 (300°)	4.98%	99.17%

For each functional direction (FD), the curvature mean relative error and the orientation accuracy are reported.

screen, whereas with the sleeve on, the camera feedback is enhanced by the GUI, providing information on the force applied and the status of the actuators (inflating/deflating), similar to the in-vitro test (**In-vitro tests**). For each trial, in addition to the navigation time, the mental and physical workload of the procedure was measured by the NASA TLX[56]. This method evaluates the overall human workload experienced during specific tasks by assessing six sub-scales: Mental Demand (MD), Physical Demand (PD), Temporal Demand (TD), Effort (E), Performance (P), and Frustration (F). Higher ratings on these sub-scales indicate that the task caused greater discomfort and required a heavier workload for the individual. Conversely, a lower TLX score suggests a less taxing workload with minimal discomfort, suggesting that the user performed the task well based on their own assessment. This evaluation was performed both for the control scenario, and subsequently when the sensor is attached to the endoscope during navigation. The learning curve of each user was calculated as the reduction in time taken to perform the colonoscopy with and without the device attached, across the five trials. This metric is ultimately important to ensure that the soft robotic sleeve can be integrated in the clinical workflow without significant learning and adaption from the endoscopist, compared to traditional colonoscopy. In Fig. 6B, two resulting force plots are shown as an example, one from a novice user (novice 1 trial 2), and one from an expert user (expert 1 trial 4). It is worth noticing that in both cases, the actuation is triggered multiple times by a force equal or greater than 5 N.

The learning curve, navigation times, and NASA TLX results are shown in Fig. 7. The learning curves for the tests with and without the soft sleeve have a downward trend as the number of trials increases, both for novice users (Fig. 7A) and experts (Fig. 7B). The average learning curves among all users combined are reported in Fig 7C. In the sleeve case, the average navigation time starts from an initial value of 70.71 ± 20.3 s, and decreases to a final value of 47.14 ± 14.3 s by trial 5. Without the sleeve, the average navigation time decreases from 56.71 ± 11.21 s in trial 1 to 39 ± 12.28 s in trial 5. This data shows that the introduction of the soft robotic sleeve into the clinical workflow does not negatively impact the learning curve. Looking at the average navigation time across all trials, novice users take 45 ± 6.62 s to complete the procedure in the control scenario, and 66.8 ± 7.59 s with the sleeve on (see Fig. 7D). This difference can be due to the inexperience and unfamiliarity of the novice users with the test. Expert users instead complete the procedure with an average time of 46.66 ± 7.59 s without the sleeve and 39.33 ± 8.86 s with the sleeve on (Fig. 7E). Interestingly, for the expert users, the average navigation time is lower in the sleeve case, showing that, after performing the control trials, they quickly adapt to the robot without needing additional time to perform the procedure. Finally, combining all the users, the average navigation time is 45.65 ± 5.35 s without the sleeve, and 55.05 ± 7.36 s with the sleeve (Fig. 7F). We conducted Wilcoxon Sign-Ranked Test on the navigation time datasets with/without sleeve for only novice users, only experts, and all the users combined. We found no statistically significant difference among novice and expert users, and when considering all the users combined. The average NASA TLX score for the novice users is 56 ± 29.36 in the control case and 53.24 ± 26.65 in the sleeve case (Fig. 7G). For the experts, the TLX score is 41.2 ± 32.87 in the control case and 35.86 ± 19.62 in the sleeve case (Fig. 7H). The lower score in the sleeve case indicates that the robot does not add workload and it is well accepted by the endoscopists. The average TLX score combining all users is shown in Fig. 7I and it is equal to 49.66 ± 20.89 without the sleeve, and 45.79 ± 17.53 with the sleeve. In particular, the major contributing aspects to the TLX score are physical demand (PD) and Effort (E) for novices (Fig. 7J) and mental demand (MD), temporal demand (TD), and effort (E) for the experts (Fig. 7K). The average sub-score with all the users is shown in Fig. 7L. By performing Wilcoxon Sign-Ranked Test on the TLX datasets, we found no statistically significant difference among novices, experts, and all users combined. This suggests that the mental and physical workload of the navigation task is comparable in the sleeve and no-sleeve scenario.

In-vivo evaluation

The performance of the soft robotic sleeve in-vitro and ex-vivo showed a successful integration of the robot with existing endoscopic tools, and a low impact on users' workload and navigation time. However, to achieve a comprehensive characterization of the robot and assess its potential clinical impact in real-world scenarios, animal testing was essential. This critical step allowed us to thoroughly examine the robot's usability and uncover any possible outcomes or risks associated with its interaction with living test subjects. The insights gained from this phase are invaluable for ensuring the robot's effectiveness and safety in clinical settings. Given the similarity between human and porcine gastrointestinal functionality and composition[57], two female pigs (Yorkshire, 30 Kg) were used for this evaluation.

We conducted a first session with two expert users, and a second session with one user repeating the test. In each session, the swine was anesthetized and supported with mechanical ventilation, with its physiological condition continuously monitored, specifically blood oxygenation (%) and heart rate (bpm). Details about the animal preparation are reported in **In-vivo testing setup**. To perform the navigation, the distal portion of the colon was used, extending for about 50 cm from the rectum, before the start of the helicoidal section. In each session, each user performed five control colonoscopy trials without the soft robotic sleeve attached on the endoscope, and subsequently five trials with the sleeve integrated on the tool ($n = 15$ total trials for each scenario). Similar to the ex-vivo tests (Section **Ex-vivo tests**), the time taken to perform each trial was recorded, as well as the internal endoscopic camera view and the contact force and actuation data, also displayed in real-time on the GUI (see Supplementary Video 6). NASA TLX metric was collected for all users both for the control and the robot trials. The endoscopy unit test setup is shown in Fig. 8A, where the main components are highlighted. The soft robotic sleeve platform is placed on a movable cart in order to be easily moved to the best location for the clinician, as well as the colonoscopy tower. In Fig. 2.8B, the soft sleeve mounted on the endoscope is visible, in its deflated and inflated state. When the soft sleeve is mounted on the endoscope, the overall thickness of the system increases by about 5.5 mm, as mentioned in **Soft Robotic Sleeve Design**. In the in-vitro and ex-vivo setups, the entrance of the colon is simulated by a relatively large opening, while in the in-vivo scenario, the animal anal sphincter is relaxed, but closed. Therefore, it is important to ensure that, during the entrance, the sleeve is tightly wrapped along the endoscope, without detaching or sliding back. In both sessions, throughout all the tests, the soft robotic sleeve proved to be firmly attached to the endoscope, and the entrance in the colon was smooth. The soft sleeve sensed contact forces throughout all the trials, and inflation was triggered multiple times (see Supplementary Fig. 10). No sign of malfunction or fiber detachment was detected. Prior to the beginning of the experiment, we noticed a rectal prolapse on the second animal, possibly due to frequent bowel movements caused by laxatives (Miralax) used for bowel preparation in the weeks before the test. However, as this condition is unrelated to the experiment, it didn't influence its outcome. In fact, the second swine exhibited comparable baseline vital signs (heart rate and oxygen saturation) to animal 1, and no sign of discomfort was visible. The average learning curve for all the users is reported in Fig. 8C. The control tests average navigation time goes from 21.12 ± 3.66 s in trial 1, to

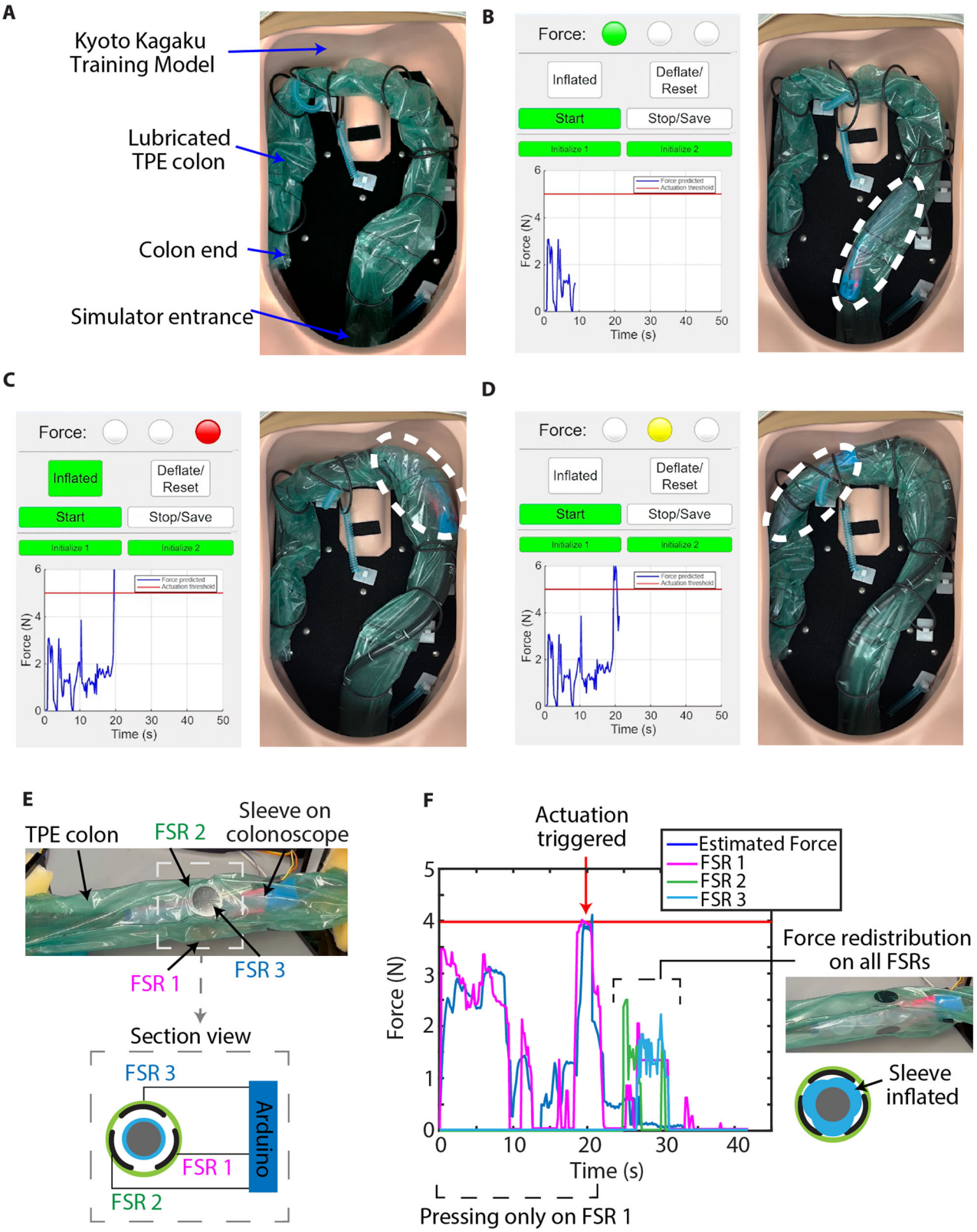

Fig. 5 | In-vitro validations. A Setup with a TPE colon inserted in a Kyoto Kagaku simulator. **B** Low force sensed and green indicator displayed (F < 3 N). **C** An excessive force is reached: the indicator turns red and the actuators starts inflating. **D** A warning zone with medium-high force (3 N ≤F < 5 N) is reached and the indicator turns yellow. **E** Three FSR sensors are bonded to the internal lumen for the force redistribution experiment. **F** Validation of redistribution: starting by pressing on one specific sensor (FSR 1), inflation is triggered, and the other two sensors start experiencing force (FSR 2 and 3).

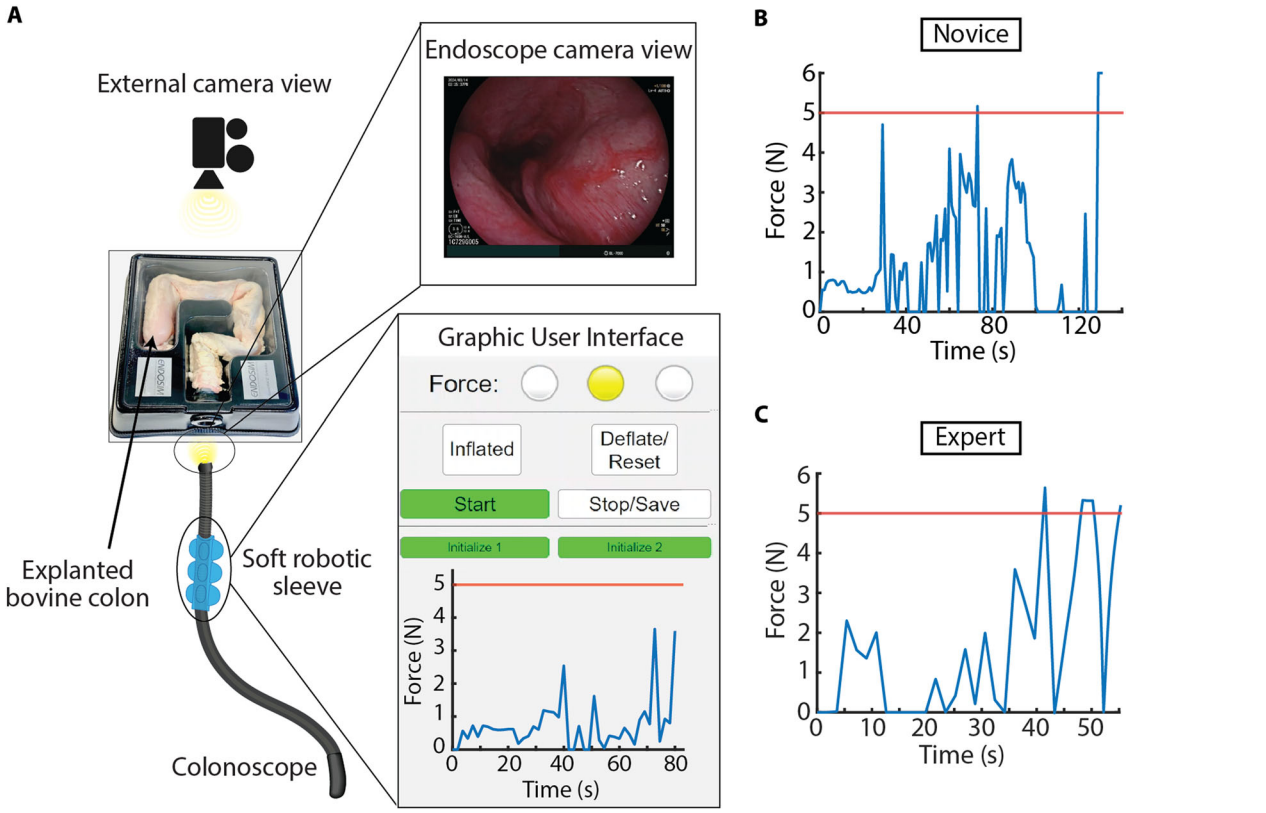

Fig. 6 | Ex-vivo validation. A Test setup including the ColoEASIE-2 Simulator with the bovine tissue placed inside it, the endoscope with the robot mounted on, the internal and external camera views, and the GUI view. Examples of tests performed by **B** a novice user (novice 1 trial 2), and **C** an expert user (expert 1 trial 4), showing the force estimated from the soft sleeve over time.

16.66 ± 2.62 s in trial 5. Similarly, the sleeve tests average navigation time starts from 27.8 ± 11.1 s in trial 1, decreasing to 18.14 ± 2.6 s. The downward trend of the learning curves confirms an easy integration of the robot into the procedure, without the need to acquire new skills by the clinicians. The average navigation time in the control tests is 18 ± 1.45 s, while in the sleeve tests it 21.6 ± 2.93 s (Fig. 8D). Although the average difference found is only 3.6 s, we found statistically significant difference from the Wilcoxon Sign-Ranked Test ($p < 0.05$). However, given that the learning curve in the sleeve scenario still has a downward trend, we believe this increase should not negatively impact the overall procedure. NASA TLX scores were calculated for each user. User 1-session 1 assigned a score of 20.3 for the control trials, and a score of 36 for the sleeve trials (Fig. 8F). User 2-session 1 instead, assigned a score of 59 for the control trials, and a score of 68 for the sleeve trials (Fig. 8G). The score for user 1-session 2 resulted the same with and without the sleeve, equal to 54. The TLX sub-score of the users combined is showed in Fig. 8E. The main contributing factors to the sub-score are mental, physical, temporal demand, and effort. However, we found no statistically significant difference in the TLX datasets of the no-sleeve/sleeve cases from the Wilcoxon Sign-Ranked Test. These promising results show a minimum impact of the soft sleeve on the mental and physical workload of the users.

To evaluate potential stress or discomfort, for each animal we compared the average heart rate and blood oxygenation before and after the start of each trial, with the start being coincident with the insertion of the endoscope in the rectum. These parameters are commonly monitored during anesthesia procedures as they can provide insights into assessing risks and distress[58–60]. The data was analyzed both for the control scenario, and the sleeve scenario, by averaging the values collected for the two expert users in the first animal session, and the one expert user in the second session. In Table 3, the vital signs percent change before and after the insertion of the endoscope are reported, for both testing sessions. For the first animal model, the insertion of the endoscope in the rectum did not cause significant change in the animal heart rate both in the control trials, resulting in 0.31% of bpm increase, and also in the sleeve trials, resulting in an increase of 0.05% of bpm. The blood oxygenation was also constant during the whole testing session, decreasing by 0.19% in the control trials, and by 0.02% in the sleeve trials. For the second animal model, similar results show no significant changes in the animal vital signs. Specifically, the heart rate increases by 0.22% bpm after the endoscope insertion during control trials, and decreases by 0.36% bpm during the sleeve trials. Blood oxygenation decreases by 0.07% in the control trials, and remains constant during the sleeve trials. These results ensure that, in both testing sessions, the presence of the soft robotic sleeve did not cause additional trauma or harm to the animal, during the endoscope insertion and throughout the navigation. This aspect represents a first step for the purpose of our robotic platform to reduce patient discomfort during colonoscopy.

The in-vivo sessions validated the seamless integration of the soft robotic sleeve in the clinical procedure, enhancing functionalities of traditional endoscopic tools with continuous contact force monitoring and automatic pressure redistribution. The robotic platform developed was smoothly transported and installed in the endoscopy unit, showing great promise as a portable compact system that could potentially be widely used in colonoscopy, both for training and clinical purposes.

Discussion

We developed a disposable soft robotic sleeve that can be directly implemented onto commercially available colonoscopes and can exploit redundant optical sensors to monitor its own shape, and ultimately detect distributed loads. Furthermore, our system is able to automatically inflate and distend the colon tissue, reducing potential tissue damage, while maintaining the ability to continue navigating through the colon lumen. It features a GUI that can inform the clinician on the level of force applied, and the status of the actuators in real-time.

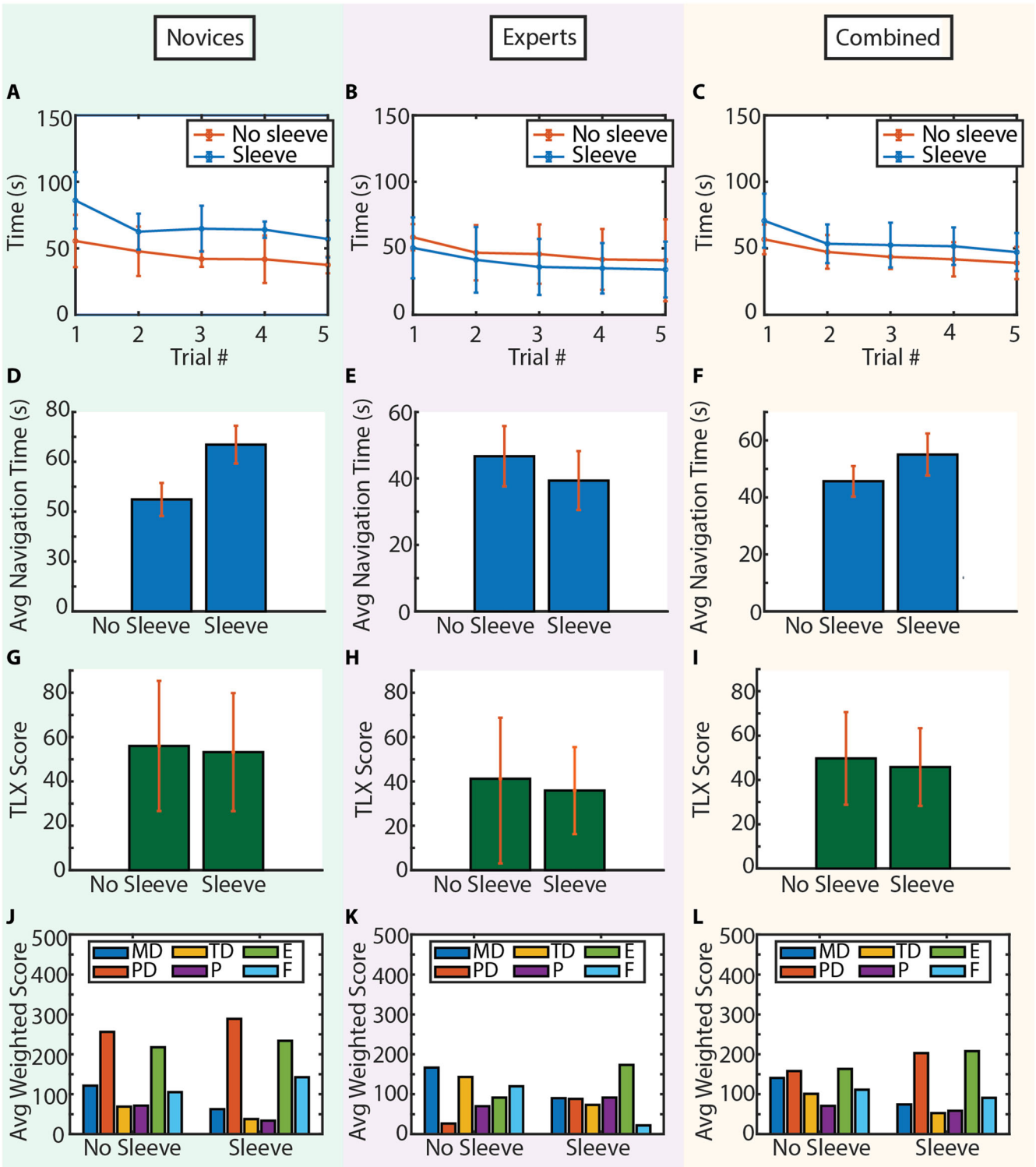

Fig. 7 | Ex-vivo metric. A–C Learning curves for novices, experts, and all users combined (mean ± standard deviation for each trial). **D–F** Average navigation times for novices, experts, and all users combined (mean ± standard deviation for all trials). **G–I** Average NASA TLX score for novices, experts, and all users combined (mean ± standard deviation for all trials). **J–L** TLX sub-scores for for novices, experts, and all users combined.

Despite the choice of the sleeve strategical location immediately behind the endoscope steerable tip, in order to protect the area where the first high forces would likely occur (as mentioned in **Soft Robotic Sleeve Design**), both the tip and the passive section behind the sleeve are uncovered by our robot, and thus exposed to potential critical contact. To address this limitation, multiple sleeves along the colonoscope could be explored, or the length of each device could be increased, in order to cover more endoscope surface and protect the tissue. However, the use of multiple sleeves would require a reorganization and a potential reduction of fibers and actuation cables exiting from the robot's base, in order not to interfere with the navigation path during testing. If the sleeve length increases, calibration for shape and force estimation will have to adapt to the new dimensions, potentially requiring a stronger light source for the longer optical path. The sensor's behavior will remain consistent unless the length exceeds the limit

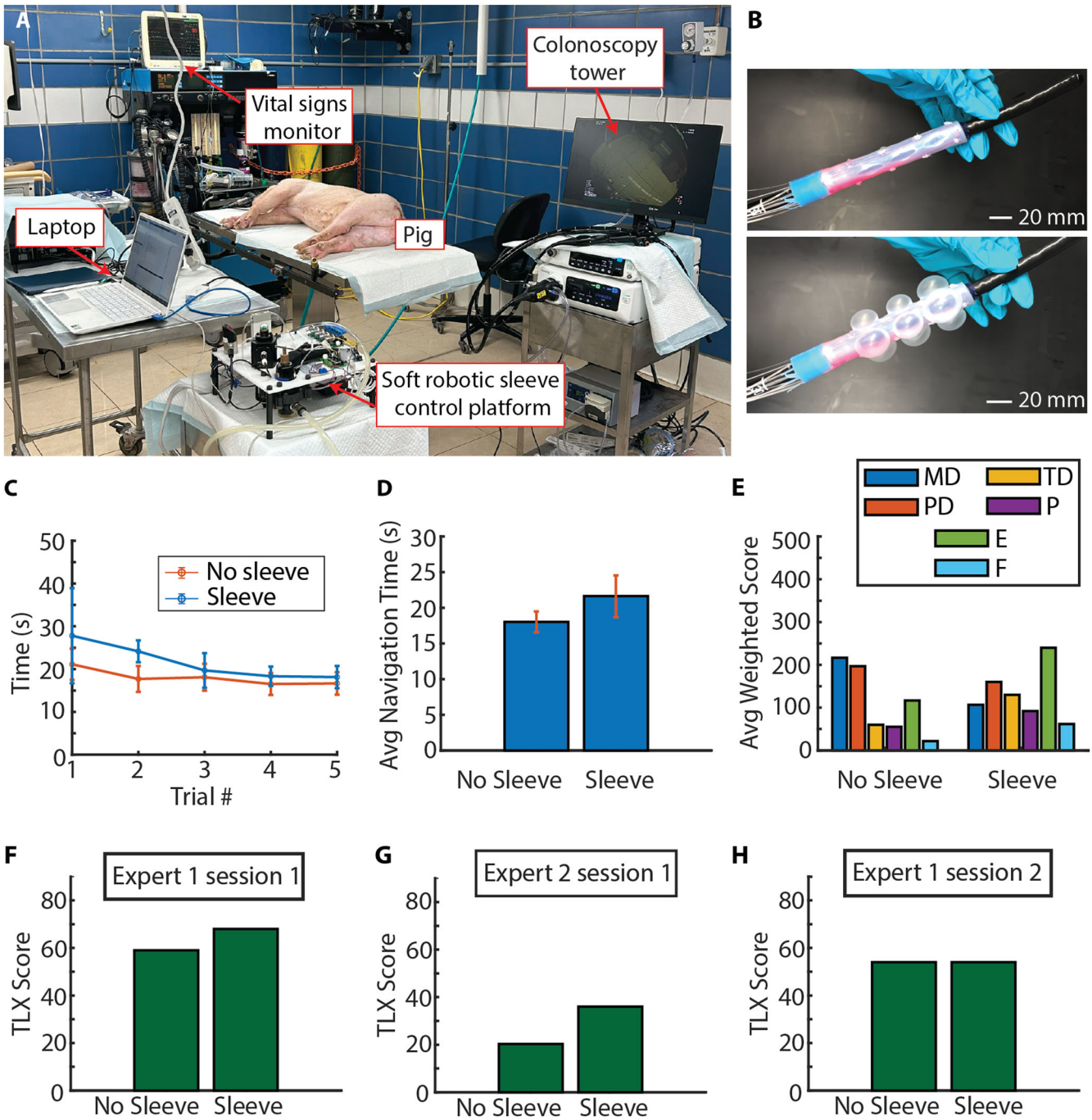

Fig. 8 | In-vivo testing. A Endoscopy unit setup. The animal is under anesthesia and its vital signs are continuously monitored. The sleeve control box is placed on a movable cart next to the operating table, as well as the colonoscopy tower. A laptop is connected to the control box to record the robot data during the navigation. **B** Soft robotic sleeve on the colonoscope, in its deflated and inflated state. **C** Average learning curves for the users with and without the sleeve attached to the colonoscope (mean ± standard deviation for each trial). **D** Average navigation times with and without soft sleeve (mean ± standard deviation for all trials) only differ by 3.6 s (Wilcoxon Sign-Ranked, $p < 0.05$). **E** Average TLX subscores for the users combined. **F**, **G**, **H** TLX total scores for each user separately.

where the constant curvature assumption is no longer valid. In such cases, alternative models like piecewise constant-curvature[55] or discrete Cosserat approaches[61], along with revised calibration methods, would be necessary. Additionally, at this stage, the system provides information only about contact intensity, and force localization has not been explored. While this could represent a limitation in certain clinical scenarios where more detailed guidance may be required, contact localization was not the focus of this study, as our primary goal was to ensure the system's ability to detect and respond to excessive forces that could lead to tissue damage during colonoscopy. Incorporating localization capabilities will require exploring different sensor designs, calibration techniques, and data-driven models, and future iterations will focus on investigating these aspects in order to expand the system's clinical applicability.

The use of redundant sensors and the decoupling algorithm that we developed allow the robot to discriminate between optical losses due to bending in the 3D space, and optical losses due to external loads, with a high accuracy. This is crucial since the actuators inflation needs to be triggered only when an excessive force is applied to the colon tissue, and not simply by bending the system. A jitter effect is noticeable in the real-time shape estimation of the robot, due to sensor resolution limitations and 3D space

Table 3 | Vital signs of Swines

Swine 1		Heart rate change (bpm)	Blood oxygenation change
	Control trials	0.31% increase	0.19% decrease
	Sleeve trials	0.05% increase	0.02% decrease
Swine 2			
	Control trials	0.22% increase	0.07% decrease
	Sleeve trials	0.36% decrease	no change

Change of heart rate and blood oxygenation before and after the insertion of the endoscope into the animal rectum, both for control and sleeve trials. Each value is averaged among five trials and two users for swine 1, and 5 trials of one user in swine 2. No significant change has been observed for both animals.

discretization, as analyzed in **Shape reconstruction validation**. Nonetheless, as our goal for the soft sleeve is to ultimately detect contact forces on its surface and trigger actuators as needed, the shape prediction serves as an intermediate step to enable accurate force estimation, and the behavior observed, while noticeable, does not significantly affect this estimation or the overall functionality of the system.

In terms of force estimation, our design focused only on the detection of contact forces acting normally to the tissue surface, rather than more complex loading, such as including shear effects. This decision was guided by the clinical significance of normal forces and their impact on patient safety during colonoscopy, as they have been well-documented to cause severe adverse effects, including perforation and trauma[50–54]. Conversely, shear strains on the colon tissue have been demonstrated to be significantly lower than axial strains, and therefore negligible[62]. This aspect supports our focus on normal contact forces in the robot design.

Due to their nature, the compliance of the soft actuators enables the sleeve to safely navigate also in irregular conditions. The inflation mechanism is fully controllable by the endoscopist and it is possible to reduce the chambers pressure as desired, or turn the inflation system completely off. The operative pressures needed to inflate the chambers at their maximum expansion are comparable to similar devices in the literature [30,33,38–40], therefore, the robot resides in the same safety range. Moreover, being single-use, our soft robot is advantageous for preventing cross-contamination and minimizing the transmission of infections between patients. In fact, by eliminating the risk of human error in the sterilization process, our disposable "add-on" ensures a consistently sterile environment and enhances procedural efficiency by reducing the time required for cleaning and reprocessing instruments.

Through the in-vitro experiments, we were able to test the feasibility of the robotic platform in a simulated environment, fine-tune parameters such as inflation and deflation time and actuators pressure, ensure repeatability of the sensor decoupling algorithm, and ultimately prove the redistribution of force when the actuators are triggered. Ex-vivo tests conducted by both novice and expert users validated the capability of the sleeve to navigate in a real tissue, and its seamless integration in the clinical workflow of colonoscopy. The user study performed provided valuable feedback on the clinical benefit of having the soft robotic sleeve enhancing traditional colonoscopy, also confirming the presence of high contact forces in the procedure. The in-vivo evaluation further validated the safety, ease of use, and the potential clinical benefit of the soft robotic platform in a living being, demonstrating no workflow disruption and showing that the animal tolerated the procedure well. In both the ex-vivo and in-vivo environments, the promising results show not only a minimal impact on the procedure time and learning curve, but also no significant impact on the NASA TLX scores, along with no visible tissue damage or perforation.

Regardless of the clinical benefit, this work also shows the potential of soft optical waveguides capabilities. These type of sensors are easy to manufacture, low-cost, and versatile, compared to other types of optical sensing, such as FBGs (Fiber Bragg Grating)[63,64], and FOSSs (Fiber Optic Sensing System)[65], that result in complex, expensive, and bulky solutions. Additionally, the implementation of contact force amplifying indenters in our design allows for the multi-modal nature of the waveguides to be enhanced and utilized in a free, open, unstructured environment. The fabrication process has proven repeatability of prototypes, without any disconnection between the soft WGs and the rigid plastic optical fibers, which is a critical aspect for the functioning of the whole system. In addition, the robot durability was validated successfully as each robot prototype was used for at least five tests without signs of malfunctioning, degradation, or optical fiber disconnection.

In the future, we plan on performing additional in-vivo studies on porcine models, to further validate the robot functionalities and its efficacy across a larger number of users. We will continue collecting feedback from the clinicians, as well as tune design aspects and functionalities of the robotic platform based on their needs. Clinical studies will be performed to further evaluate the system's effectiveness in real-world scenarios. As part of this effort, we plan to develop new metrics for assessing patient pain and discomfort during the procedure, such as nurse-reported comfort levels (NRCL). These metrics will provide a more comprehensive understanding of the device's impact on patient experience, enabling us to ultimately evaluate its full clinical benefit. In terms of fabrication, some aspects could be optimized in order to reduce manufacturing time, such as implementing a single cylindrical mold to create the robot body, instead of molding three flat layers and manually sewing them together to create a tubular shape (see **Fabrication**). On this note, further improvements could involve the implementation of a wireless system with all the electronics on-board, miniaturized, and well protected from body fluids. In conclusion, the proposed soft robotic sleeve opens promising avenues for safer colonoscopies procedures, being a low-cost, fully-soft, disposable "add-on" that can be mounted on commercial endoscopes and accurately detect and respond to contact forces, resulting in an important step for the diagnosis and treatment of colorectal cancer.

Methods

Soft robotic platform design

The five WGs of the soft robotic sleeve are *U*-shaped and have a square cross section of 750 μm x 750 μm (see Supplementary Fig. 11A). The radius of curvature in correspondence to the *U* section is 3 mm and 5 mm for the bending layer and the contact layer, respectively (see Supplementary Fig. 11B). NOA 65 was selected as the core material for the WGs due to its high refractive index, low viscosity for injection, low elastic modulus and high flexibility, and for its ease in fabrication as it is UV curable. Circular POFs with a 750 μm external diameter (Industrial Fiber Optics Inc.) were chosen to interface with the soft cores of the sleeve. In this way, all the light emitted from the POF can be captured by the square WG end. Each pneumatic actuator line is composed of three oval chambers with a major axis of 30 mm and a minor axis of 8 mm (see Supplementary Fig. 11B), and an actuator membrane of 1.25 mm. Their shape was selected as it maximizes the expanded height and surface area while minimizing the impact on the WGs due to lateral expansion of the actuators against the WG channels. The chambers are connected by a 1 mm channel, which is connected to a 1.65 mm tubing (Micro-Renathane 0.065" x 0.030", Braintree Scientific Inc.) to enable actuation. The contact amplifying indenters are elliptically shaped with a 2 mm major axis, a 1 mm minor axis, and a 1 mm height (see Supplementary Fig. 11C). For the optical circuit (Supplementary Fig. 2), five red 650 nm LEDs (IF-E99B, Industrial Fiber Optics) are utilized as light source emitters, while five photo-transistors (IF-D92, Industrial Fiber Optics) are used as receivers to read the sensor signals. Each photo-transistor is connected to a potentiometer to adjust the bandwidth of the sensor into the required range for each WG. The pressure control hardware components are also schematized in the orange section of Supplementary Fig. 3.

Fabrication

To fabricate the soft robotic sleeve, we utilized a layer-by-layer approach, with subsequent wrapping in a cylindrical shape to fit around standard

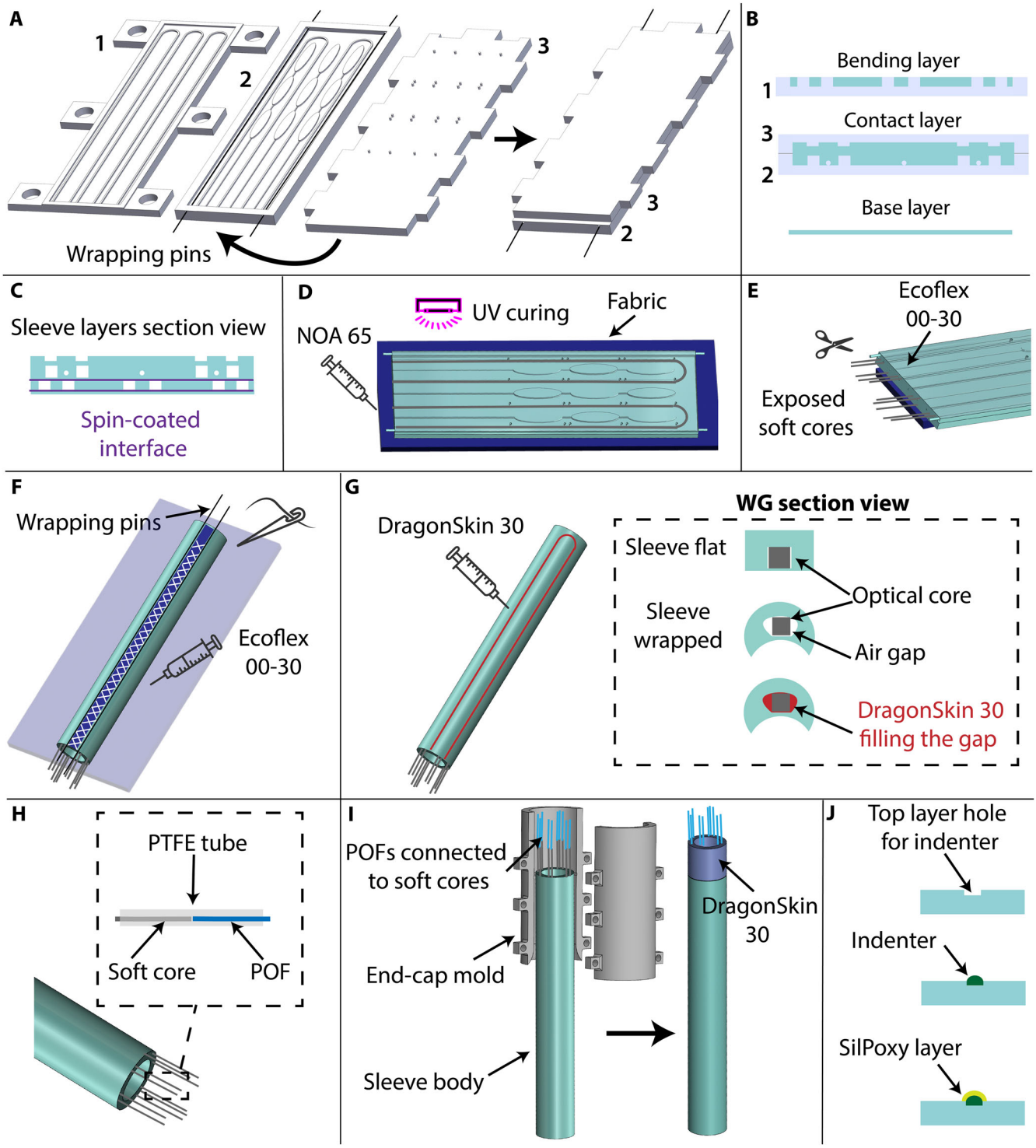

Fig. 9 | Soft sleeve fabrication. A Three aluminum molds are machined for the bending layer (1), contact layer(2), and mask for indenters (3). Silicone is poured into (1) and (2). (3) is placed on top of (2), and all the molds are degassed and cured. **B** The base layer is spin-coated. The section view of the three layers is shown. **C** The layers are stacked together by spin-coating steps. **D** The sleeve body is bonded to a fabric and NOA 65 is injected into the 5 channels to create the WG cores, and UV cured. **E** A portion of the cores is exposed. **F** The sleeve is wrapped into a cylinder and silicone is injected into the seam to reinforce it. **G** Anti-buckling layer injection. **H** The soft cores and the POFs are encapsulated in a PTFE tube. **I** The end-cap is molded to secure the soft-rigid connection. **J** Indenters placement.

commercial colonoscopes. Three aluminum molds are fabricated by using a CNC (Computer Numerical Control) machine. The first one is used to create the internal layer of the sleeve (or bending layer), containing three WG channels (mold 1 in Fig. 9A). The second mold creates the external layer (or contact layer), containing two WGs and the actuator chambers (mold 2 in Fig. 9A). A third mold, containing the pins to define the location of the indenters, is used as a "masking" mold for the contact layer, in order to create the precise locations directly above the contact WGs where the indenters will be later incorporated (mold 3 in Fig. 9A). The bending layer mold is filled with Ecoflex™ 00-30, degassed, and cured (20 min at 70 °C). Two lateral 1 mm pins are inserted into the contact layer mold, in order to create channels for the later wrapping step (wrapping pins in Fig. 9A).

Ecoflex™ 00-30 is poured into the contact layer mold, degassed, and cured (20 min at 70 °C). The contact layer mold is sandwiched with the "masking", and subsequently cured (Fig. 9A). A thin layer of silicone is spin-coated and cured, in order to create a 0.25 mm base layer to close the internal mold. The section view of the three layers, and their molds, is visible in Fig. 9B. The layers created (base layer, bending layer, and contact layer) are then stacked together through spin-coating steps, that create bonding interfaces 0.1 mm thick (Fig. 9C). This step creates the sleeve soft body. The latter is then bonded to a flexible fabric with silicone adhesive (SilPoxy), and NOA 65 is injected into the five channels and UV cured, to create the cores of the WGs (Fig. 9D). Next, a small 10 mm portion of the newly cured optical core is exposed by cutting the surrounding silicone cladding (Fig. 9E). The sleeve is then wrapped and its side edges are tightly sewed together. To help with this step, two 1 mm pins are inserted into the side channels previously created in the bottom layer, and Ecoflex™ 00-30 is used to reinforce the seam (Fig. 9F). The wrapping pins are then removed after the curing process. Due to the stretching cause by the wrapping, the optical channels are now prone to buckling when bent, since there is an air gap between the optical core and the cladding. To address this issue, Dragon Skin™ 30 is injected into the channels to create an anti-buckling layer which supports the core region and fills in the air gap (Fig. 9G). The previously exposed optical core section, protruding from the body of the sleeve, is then interfaced and bonded with commercial plastic optical fibers through a PTFE tube encasing (Fig. 9H). To protect the optical interface during motion, a Dragonskin™ 30 end cap is molded around the base of the sleeve, avoiding decoupling of the optical fiber connection (Fig. 9I). Further, this end cap is dyed cyan in order to trap the red LED light sent into the WG cores to both prevent signal cross talk and to block ambient light noise. The final step of the soft sleeve fabrication is to place the 3D printed indenters into the previously created holes on the top layer. The indenters are bonded on the robot with SilPoxy, that creates a soft interface with the colon tissue, avoiding sharp contact and potential damage, but also ensuring contact force transmission into the optical cores (Fig. 9J).

Curvature and orientation calibration

To study the response to bending of the five WGs in the 3D space, the system was initially divided arbitrarily in twelve different orientations, spaced 30° apart, as shown in Supplementary Fig. 4. This fine division was established to better capture the signals behavior when bending the sleeve in 3D, and to investigate potential patterns in responses. For each orientation, the robot was placed in a calibration platform and bent up to 15 m^{-1} (≈140°) with steps of 1 m^{-1}, and the corresponding signal of the five WGs was recorded (setup shown in Supplementary Fig. 12). Therefore, for each orientation, the recorded voltages were converted into optical losses according to Eq. (1) and plotted versus curvature. The twelve resulting plots are shown in Supplementary Fig. 5. A pattern in the WGs responses is visible, due to the partial symmetry of the sensor geometry layout. In particular, there are similar responses going from Orientation 30° to 180°, and from 210° to 330°, and back to 0°. Given this symmetrical similarity of the WGs responses across the bending directions tested, we further approximated the sleeve orientations into four functional directions (60°, 120°, 240°, 300°), which have unique response profiles, and thus can well represent the sleeve orientation as four sections of the 3D space. This division ensured that the sleeve algorithm is able to accurately discriminate between each functional direction, since two adjacent profiles that have very similar responses would not be able to be differentiated (for instance orientation 120° and 150° of Supplementary Fig. 5). These four orientations, symmetrical with respect to the horizontal and vertical axes of the sleeve, were chosen to maximize the force amplification from the indenters, and with the assumption that, when the sleeve is bent in a specific direction, the possible contact forces will occur on the diametrical opposite one (for instance, bending towards 60° corresponds to pressing on 240°). Ultimately, these profiles are used by the decoupling algorithm to reconstruct the robot shape. While this approach results into an approximation of the 3D space, the primary goal of the system is to accurately detect and respond to contact forces, rather than focusing on achieving high-resolution shape reconstruction. For this reason, the discretization of the sleeve orientations into four distinct directions proves to be a practical and efficient solution, enabling the system to maintain sufficient accuracy for the intended application of force detection. Additionally, our design assumes that the contact forces are located on the outer curve of the colonoscope. This might not be true in every clinical scenario, however, our navigation tests confirmed the presence of high contact forces on the outer portion of the tool, mostly when the user is bending the endoscope and pushing it against the colon wall (see the in-vitro navigation of Supplementary Movie 4).

Contact force calibration

The sleeve was initially subjected to distributed loads for the four FDs chosen, to determine the losses due to contact interactions in different scenarios. The robot was placed in a 3D printed fixture, at a curvature of 10 m^{-1} (≈92°). A curved 3D printed attachment was fabricated, having matching curvature with the sleeve, to simulate distributed loads applied by the colon tissue. An Instron testing machine (5943 Instron, USA) was used to apply gradually increasing loads on the soft sleeve up to 6 N, while recording the signals from the five WGs. The resulting plots are visible in Supplementary Fig. 6, showing that, depending on the robot orientation, the WGs experiencing major loss are the two external WGs on the contact layer, as expected. These calibrations are utilized to determine the amount of force that is being applied on the colon wall by the user during navigation.

Actuators characterization

The actuators were inflated to test their effects on the sensor signals and to determine the settling time for the sleeve WGs to return to their baselines. The characterization was performed both with the robot in a straight configuration, and bent at 10 m^{-1} curvature, to evaluate potential curvature influence on the responses and evaluate if the same inflating pressure is reachable. To calculate the settling time, the actuators are first inflated to their maximum expansion and the losses of the WGs are monitored. After pressure is released, the actuators starts deflating, and the time taken for the sensors signals to go back to their baselines is measured. As shown in Supplementary Fig. 13A, the total loss (as the sum of the five WGs losses) drops in about 3 seconds, meaning a quick return of the sensors to their baselines after inflation. Therefore, a settling time of 3 s is implemented into our control code to ensure complete settling for the sensor before continuing to sense force (see **Soft Robotic Sleeve Design**). To characterize the actuators, a test was performed by controlling the volume of air inserted in the three actuator lines, recording the corresponding pressure with a pressure sensor, and the height of expansion reached. The total volume inserted was 50 ml with 5 ml increments at 55 ml/min, corresponding to a maximum pressure of about 25 kPa. The loss versus pressure trends are reported in Supplementary Fig. 13C and E for straight and curved configuration, respectively. As expected, all of the five WGs are affected by the actuators expansion, experiencing loss up to 7 dB when straight, and 4 dB when curved. The maximum height reached by a single actuator line was 12.7 mm in a straight configuration and 13 mm in the bent configuration (see Supplementary Fig. 13D and F, respectively). This confirms that the actuators performance is not inhibited by the bending of the sleeve. Due to the symmetry of the actuators design, the maximum inflation adds ≈ 26 mm to the sleeve diameter, ensuring a good contact with the colon wall for pressure redistribution.

In-vivo testing setup

Approval of all ethical and experimental procedures and protocols was granted by the Institutional Animal Care and Use Committee of PARF (Pine Acres Rabbitry Farm and Research Facility), OLAW Assurance # A3834-01, and Boston University's IRB protocol # 5884X. Two female Yorkshire swine of 30 Kg were used for animal testing. For all animals, intramuscular buprenorphine (0.3 mg/mL) was administered at a dose of 0.01 mg/kg just prior to anesthesia induction to minimize discomfort. Vascular access was then obtained via a peripheral intravenous catheter (e.g., ear vein), followed

by intravenous administration of Xylazine (100 mg/mL) at a dose of 2.2 mg/kg. All animals underwent endotracheal intubation. Isoflurane gas anesthesia was administered at 0.1–5.0% to maintain general anesthesia. Depth of anesthesia was monitored by a trained veterinarian, focusing on the following signs: overall appearance, vital signs (pulse rate and O_2 saturation), palpebral and/or withdrawal reflexes, jaw tone.

Data availability

Datasets generated during the current study are available from the corresponding author on reasonable request.

Received: 7 November 2024; Accepted: 26 April 2025;
Published online: 13 June 2025

References

1. Siegel, R. L., Wagle, N. S., Cercek, A., Smith, R. A. & Jemal, A. Colorectal cancer statistics, 2023. *CA: Cancer J. Clin.* **73**, 233–254 (2023).
2. Siegel, R. L., Giaquinto, A. N. & Jemal, A. Cancer statistics. *CA: Cancer J. Clin* **74**, 12–49 (2024).
3. Santucci, C. et al. European cancer mortality predictions for the year 2024 with focus on colorectal cancer. *Ann. Oncol.* **35**, 308–316 (2024).
4. Siegel, R. L., Miller, K. D., Fuchs, H. E. & Jemal, A. Cancer statistics, 2023. *CA: Cancer J. Clin.* **73**, 17–48 (2023).
5. Maes-Carballo, M. et al. A comprehensive systematic review of colorectal cancer screening clinical practices guidelines and consensus statements. *Br. J. Cancer* **128**, 946–957 (2023).
6. Loeve, A., Breedveld, P. & Dankelman, J. Scopes too flexible and too stiff. *IEEE Pulse* **1**, 26–41 (2010).
7. Valdastri, P., Simi, M. & Webster III, R. J. Advanced technologies for gastrointestinal endoscopy. *Annu. Rev. Biomed. Eng.* **14**, 397–429 (2012).
8. Franco, D. L., Leighton, J. A. & Gurudu, S. R. Approach to incomplete colonoscopy: new techniques and technologies. *Gastroenterol. Hepatol.* **13**, 476 (2017).
9. Kim, S. Y., Kim, H.-S. & Park, H. J. Adverse events related to colonoscopy: Global trends and future challenges. *World J. Gastroenterol.* **25**, 190 (2019).
10. Huffstetler, A. N., Fraiman, J., Brownlee, S., Stoto, M. A. & Lin, K. W. An estimate of severe harms due to screening colonoscopy: a systematic review. *J. Am. Board Fam. Med.* **36**, 493–500 (2023).
11. Schoenfeld, P. S. & Cohen, J. Quality indicators for colorectal cancer screening for colonoscopy. *Tech. Gastrointest. Endosc.* **15**, 59–68 (2013).
12. Hsu, W.-F. & Chiu, H.-M. Cost-effectiveness of colonoscopy and related procedures: population screening perspectives. *Mini-Invasive Surg.* **6**, 1–11 (2022).
13. Manfredi, L. Endorobots for colonoscopy: Design challenges and available technologies. *Front. Robot. AI* **8**, 705454 (2021).
14. Huan, Y. & Ciuti, G. Colonoscopy robots. In *Endorobotics*, 31–59 (Elsevier, 2022).
15. Schoofs, N., Deviere, J. & Van Gossum, A. Pillcam colon capsule endoscopy compared with colonoscopy for colorectal tumor diagnosis: a prospective pilot study. *Endoscopy* **38**, 971–977 (2006).
16. Tai, F. W. D., McAlindon, M. & Sidhu, R. Colon capsule endoscopy–shining the light through the colon. *Curr. Gastroenterol. Rep.* **25**, 99–105 (2023).
17. Gounella, R. et al. Endoscope capsules: The present situation and future outlooks. *Bioengineering* **10**, 1347 (2023).
18. Zhang, J., Liu, Y., Tian, J., Zhu, D. & Prasad, S. Design and experimental investigation of a vibro-impact capsule robot for colonoscopy. *IEEE Robot. Autom. Lett.* **8**, 1842–1849 (2023).
19. Consumi, V., Lindenroth, L., Merlin, J., Stoyanov, D. & Stilli, A. Design and evaluation of the softscreen capsule for colonoscopy. *IEEE Robot. Autom. Lett.* **8**, 1659–1666 (2023).
20. Gibbons, E., Kelly, O. & Hall, B. Advances in colon capsule endoscopy: a review of current applications and challenges. *Front. Gastroenterol.* **2**, 1316334 (2023).
21. Vuik, F. E. et al. Colon capsule endoscopy in colorectal cancer screening: a systematic review. *Endoscopy* **53**, 815–824 (2021).
22. Mateen, H., Basar, R., Ahmed, A. U. & Ahmad, M. Y. Localization of wireless capsule endoscope: A systematic review. *IEEE Sens. J.* **17**, 1197–1206 (2017).
23. Chen, W., Sui, J. & Wang, C. Magnetically actuated capsule robots: A review. *IEEE Access* **10**, 88398–88420 (2022).
24. Obstein, K. L. & Valdastri, P. Advanced endoscopic technologies for colorectal cancer screening. *World J. Gastroenterol.* **19**, 431 (2013).
25. Martin, J. W. et al. Enabling the future of colonoscopy with intelligent and autonomous magnetic manipulation. *Nat. Mach. Intell.* **2**, 595–606 (2020).
26. Martin, J. W. et al. Robotic autonomy for magnetic endoscope biopsy. *IEEE Trans. Med. Robot. Bionics* **4**, 599–607 (2022).
27. Li, Y. et al. Towards semi-autonomous colon screening using an electromagnetically actuated soft-tethered colonoscope based on visual servo control. *IEEE Trans. Biomed. Eng.* **71**, 77–88 (2023).
28. Bianchi, F. et al. An innovative robotic platform for magnetically-driven painless colonoscopy. *Ann.Transl. Med.* **5**, 1–6 (2017).
29. Ciuti, G. et al. Frontiers of robotic colonoscopy: A comprehensive review of robotic colonoscopes and technologies. *J. Clin. Med.* **9**, 16–48 (2020).
30. Kim, H. et al. A sigmoid-colon-straightening soft actuator with peristaltic motion for colonoscopy insertion assistance: Easycolon. *IEEE Robot. Autom. Lett.* **6**, 3577–3584 (2021).
31. Osawa, K. et al. Self-propelled colonoscopy robot using flexible paddles. *IEEE Robot. Autom. Lett.* **5**, 6710–6716 (2020).
32. Bernth, J. E. et al. MorphGI: A self-propelling soft robotic endoscope through morphing shape. *Soft Robot.* **11**, 670–683 (2024).
33. Chen, Z., Liu, J., Wang, S. & Zuo, S. A bio-inspired self-propelling endoscopic device for inspecting the large intestine. *Bioinspir. Biomim.* **14**, 066013 (2019).
34. Li, Y. et al. Design and preliminary evaluation of an electromagnetically actuated soft-tethered colonoscope. *IEEE Trans. Med. Robot. Bion.* **3**, 402–413 (2021).
35. Chen, G., Yu, W., Wu, Y. & Zheng, J. Design and optimization of soft colonoscopy robot with variable cross section. *Cobot* **3**, 4 (2024).
36. Takamatsu, T. et al. Robotic endoscope with double-balloon and double-bend tube for colonoscopy. *Sci. Rep.* **13**, 10494 (2023).
37. Chen, J. et al. A novel inchworm-inspired soft robotic colonoscope based on a rubber bellows. *Micromachines* **13**, 635 (2022).
38. Huan, Y. et al. Flexible over-the-tube device for soft-tethered colonoscopy. *IEEE/ASME Trans. Mechatron.* **29**, 1611–1621 (2023).
39. Javazm, M. R., Kara, O. C. & Alambeigi, F. A novel soft and inflatable strain-based tactile sensing balloon for enhanced diagnosis of colorectal cancer polyps via colonoscopy. *IEEE Sensors J.* **24**, 26564–26573 (2024).
40. Borvorntanajanya, K. et al. Development of a low pressure pouch sensor for force measurement in colonoscopy procedures. In *2024 IEEE/RSJ International Conference on Intelligent Robots and Systems (IROS)*, 2366–2372 (IEEE, 2024).
41. Cianchetti, M., Laschi, C., Menciassi, A. & Dario, P. Biomedical applications of soft robotics. *Nat. Rev. Mater.* **3**, 143–153 (2018).
42. Tumino, E. et al. Robotic colonoscopy and beyond: insights into modern lower gastrointestinal endoscopy. *Diagnostics* **13**, 2452 (2023).
43. Kothari, S. T. et al. Asge review of adverse events in colonoscopy. *Gastrointest. Endosc.* **90**, 863–876 (2019).
44. Choi, J. & Drozek, D. Development of a colonoscope sheath device for colonoscopy. *J. Med. Devices.* **5**, 031005 (2011).

45. Verra, M. et al. Robotic-assisted colonoscopy platform with a magnetically-actuated soft-tethered capsule. *Cancers.* **12**, 2485 (2020).
46. Zheng, C. et al. A novel sensor for real-time measurement of force and torque of colonoscope. In *IECON 2017-43rd Annual Conference of the IEEE Industrial Electronics Society*, 3265–3269 (IEEE, 2017).
47. Dogramadzi, S., Virk, G., Bell, G., Rowland, R. & Hancock, J. Recording forces exerted on the bowel wall during colonoscopy: in vitro evaluation. *Int. J. Med. Robot. Comput. Assist. Surg.* **1**, 89–97 (2005).
48. Vajpeyi, A. et al. A novel, flexible, full-length, pressure-sensing sleeve for colonoscopes. *IEEE Sensors J.* **24**, 2513–2521 (2023).
49. McCandless, M., Gerald, A., Carroll, A., Aihara, H. & Russo, S. A soft robotic sleeve for safer colonoscopy procedures. *IEEE Robot. Autom. Lett.* **6**, 5292–5299 (2021).
50. Johnson, S. et al. How much force is required to perforate a colon during colonoscopy? An experimental study. *J. Mech. Behav. Biomed. Mater.* **91**, 139–148 (2019).
51. Korman, L. Y. et al. Characterization of forces applied by endoscopists during colonoscopy by using a wireless colonoscopy force monitor. *Gastrointest. Endosc.* **71**, 327–334 (2010).
52. Ende, A. R. et al. Objective differences in colonoscopy technique between trainee and expert endoscopists using the colonoscopy force monitor. *Digest. Dis. Sci.* **63**, 46–52 (2018).
53. Appleyard, M. N. et al. The measurement of forces exerted during colonoscopy. *Gastrointest. Endosc.* **52**, 237–240 (2000).
54. Burt, A. V. Pneumatic rupture of the intestinal canal: with experimental data showing the mechanism of perforation and the pressure required. *Arch. Surg.* **22**, 875–902 (1931).
55. Webster III, R. J. & Jones, B. A. Design and kinematic modeling of constant curvature continuum robots: A review. *Int. J. Robot. Res.* **29**, 1661–1683 (2010).
56. Hart, S. G. NASA Task Load Index (TLX). *NASA Ames Research Center* (1986).
57. Lunney, J. K. et al. Importance of the pig as a human biomedical model. *Sci. Transl. Med.* **13**, eabd5758 (2021).
58. Yoo, Y. C. Endoscopic sedation: risk assessment and monitoring. *Clin. Endosc.* **47**, 151 (2014).
59. Early, D. S. et al. Guidelines for sedation and anesthesia in gi endoscopy. *Gastrointest. Endosc.* **87**, 327–337 (2018).
60. Amornyotin, S. Sedation and monitoring for gastrointestinal endoscopy. *World J. Gastrointest. Endosc.* **5**, 47 (2013).
61. Renda, F., Boyer, F., Dias, J. & Seneviratne, L. Discrete Cosserat approach for multisection soft manipulator dynamics. *IEEE Trans. Robot.* **34**, 1518–1533 (2018).
62. Bellini, C., Glass, P., Sitti, M. & Di Martino, E. S. Biaxial mechanical modeling of the small intestine. *J. Mech. Behav. Biomed. Mater.* **4**, 1727–1740 (2011).
63. Hao, J., Zhang, Z., Wang, S. & Shi, C. 2d shape estimation of a pneumatic-driven soft finger with a large bending angle based on learning from two sensing modalities. *Adv. Intell. Syst.* **5**, 2200324 (2023).
64. Al-Ahmad, O., Ourak, M., Van Roosbroeck, J., Vlekken, J. & Vander Poorten, E. Improved fbg-based shape sensing methods for vascular catheterization treatment. *IEEE Robot. Autom. Lett.* **5**, 4687–4694 (2020).
65. Galloway, K. C. et al. Fiber optic shape sensing for soft robotics. *Soft Robot.* **6**, 671–684 (2019).

Acknowledgements

We thank the clinical fellows and the novice users who participated in our ex-vivo and in-vivo studies for their availability and precious feedback on the robot. We also thank the staff of Brigham and Women's Hospital and Pine Acres Rabbitry Farm and Research Facility (PARF) for their help on scheduling testing sessions and providing tissue samples, as well as animals for testing.

Author contributions

S.R. conceived the study and supervised the findings presented in this work. H.A. provided clinical expertise, equipment, and guidance relating to the integration of the soft robotic sleeve in the colonoscopy workflow and to the clinical significance of the project. V.D. and M.M. wrote the manuscript with inputs from all authors. V.D. and M.M. developed the final design and fabrication processes of the robot. V.D., M.M., A.G., E.C., and C.M. manufactured the robot, and performed the experimental characterizations and calibrations listed herein. V.D., M.M., C.M., and J.P. designed and manufactured the optical circuitry and control box. V.D., M.M., and M.B. contributed to the design of the contact force indenters. V.D., M.M., A.G., C.M., and J.P. participated in the ex-vivo studies, and V.D., M.M., A.G., and J.P. participated in the in-vivo sessions.

Competing interests

The authors declare no competing interests.

Additional information

Supplementary information The online version contains supplementary material available at https://doi.org/10.1038/s44182-025-00028-1.

Correspondence and requests for materials should be addressed to Sheila Russo.